Mathematics and Computers in Simulation 241 (2026) 783–804

Contents lists available at ScienceDirect

Mathematics and Computers in Simulation

journal homepage: www.elsevier.com/locate/matcom

Original articles

Nonlinear study of interacting population with increasing functional response: The significance of fear and movement

R.P. Gupta [a], Harinand Singh [a], Roberto Barrio [b,*], Arun Kumar [c]

[a] Department of Mathematics, Institute of Science, Banaras Hindu University, Varanasi 221005, India
[b] Department of Applied Mathematics, University of Zaragoza, Zaragoza 50009, Spain
[c] School of Mathematical and Statistical Sciences, Indian Institute of Technology Mandi, Mandi 175005, India

ARTICLE INFO

Keywords:
Predator–prey model
Fear effect
Bistability
Bifurcation
Turing instability

ABSTRACT

The study of hunting cooperation and fear effects is emerging as important ecological factors in population dynamics. These two features are analyzed independently in the literature by several researchers in detail. It is observed that both effects are important but poorly understood mechanisms that mediate the way predators organize ecosystems. The literature suggests that the outcomes of predator–prey interactions and their impact on ecosystems can be influenced together by these two factors. Therefore, we review the expanding body of research that integrates hunting cooperation and/or the effect of fear phenomena into the ecology of predator–prey. Our aim is to provide a framework for examining how the increasing type of functional response is affected by fear factor. The temporal dynamics, including the stability and bifurcation analysis of the system, is discussed briefly. Various parametric planes are analyzed to identify the regions of stability, instability, and bistability, along with some invariant manifolds in the phase plane that divide the basins of attraction. The temporal model is extended to the spatiotemporal framework to capture the movements of populations, and the conditions for Turing instability are derived, revealing spatial dynamics that produce various Turing patterns (spots, stripes, and mixed type) in response to the changes in fear effect and diffusion coefficients. Extensive numerical simulations are also performed to illustrate the dynamics of the model in temporal and spatio-temporal contexts.

1. Introduction

The study of ecological systems is gaining popularity among mathematicians, theoretical ecologists, and other scientists seeking to improve their understanding of the importance of ecosystems for the environment. Continuous-time models for two species are among the most frequently utilized, and they are important methods for illustrating a variety of complex population dynamics. The first mathematical model of predator–prey was introduced by Lotka and Volterra [1]. Numerous food chain models are developed and examined [2–5] with inspiration from the works of Lotka and Volterra. It is generally accepted that the prey population grows logistically in the absence of the predator. The natural growth rate and the carrying capacity are the parameters that define the logistic equation. Carrying capacity refers to the high density of a species that can support a given habitat due to limited resources [6]. The most significant key aspect of predator–prey systems is a functional response which influences the dynamics of

* Corresponding author.
E-mail addresses: ravipguptaiitk@gmail.com (R.P. Gupta), harinandsingh337@gmail.com (H. Singh), rbarrio@unizar.es (R. Barrio), arunanuj94@gmail.com (A. Kumar).

https://doi.org/10.1016/j.matcom.2025.11.009
Received 16 September 2025; Received in revised form 4 November 2025; Accepted 10 November 2025
Available online 11 November 2025

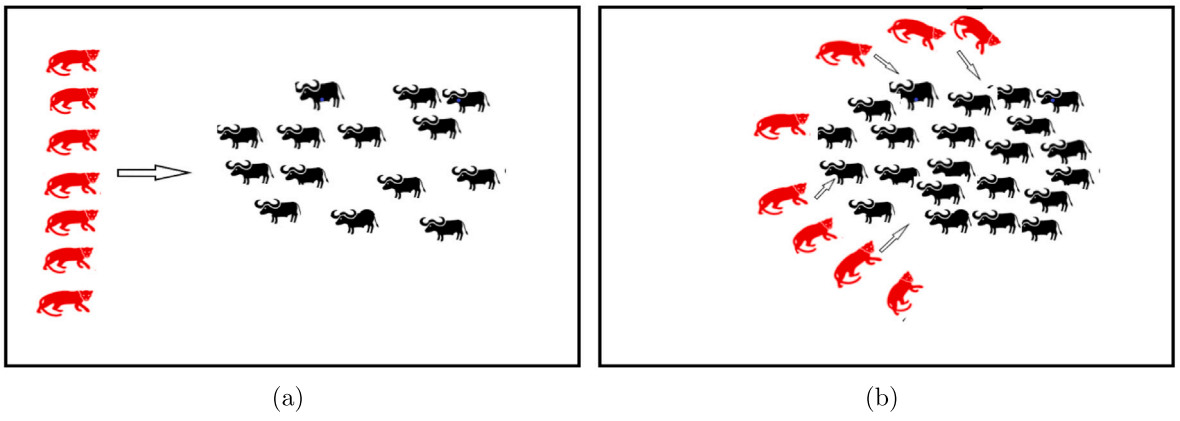

Fig. 1. The schematic illustrates how a group of predators feeding in line abreast formation could gather upon encountering a school or herd of prey. Panel (a) shows the foraging formation while (b) shows the aggregation process. This sort of behavior could in theory lead to an effective increase in encounter rate.

the models. There are several types of functional responses in ecology, such as Holling type I-III [7], Beddington–DeAngelis type [8], Crowley–Martin type [9], etc.

While deriving Holling-type functional responses, see Refs. [10,11] introduced the general response function

$$H(N,P) = \frac{a\,\mathcal{E}/P}{1 + h\,a\,\mathcal{E}/P},$$

where N and P represent the current population size of the prey and predator, respectively. The parameter a is the fraction of a prey species killed per predator per encounter, $\mathcal{E}$ is the total encounter rate between predators and prey per unit of time and h is the handling time per prey. The total encounter rate becomes $\mathcal{E} = b_0 N P$ when predators search for prey by forming a line and moving in a direction perpendicular or transverse to that line, where b_0 is the constant attack rate of the predator. In this scenario, the authors assumed that a single predator can encounter a single prey at a time, and while one predator handles the prey, the remaining continued searching for others. In contrast, when a predator comes into contact with a prey, it alerts all other predators, who subsequently gather around the prey. The authors also assumed that prey individuals group into schools, herds, or patches to escape predators before all of them are eaten. The accompanying functional response may be accurate at low/moderate predator group sizes, as accurate signal transmission from one to another is possible only if the line formation of foragers is not so long. This scenario is depicted in Fig. 1. In this case, the number of encounters between prey and predator is proportional to the number of predators, depending on the area swept in the unit of time. When the prey comes into contact with a predator, it immediately becomes an interaction with all predators, increasing the total number of encounters by a factor of P such that $\mathcal{E} = b_0 N P^2$. Based upon this assumption, Cosner et al. [10] introduced an innovative functional response:

$$H(N,P) = \frac{a\,b_0 N P}{1 + h\,a\,b_0 N P}.$$

The most significant property of this functional response is observed to be that the density of both species increases. The monotonicity and maximum value of this response function may be understood as: The hunting efficiency of predators increases when their population is large enough to support their activities [see Fig. 1(a)]. However, predation efficiency is not as good when the number of predators is too high or when predators come into contact with a school/herd of prey. This is because if the formation of the predator's feeding line becomes too long, as a result of which the transfer of signals between predators is not smooth and the prey school also counterattacks the predator [see Fig. 1(b)]. In order to enhance their biomass, predators often strive to get better at catching and killing prey, since they are dependent on it for survival. Although rivalry for resources is an essential component of predator–prey interaction, when using a particular technique, such as hunting, many species also use the technique of cooperation, which involves two or more individuals working together to achieve a similar goal. Several species exhibit hunting cooperation behavior in real life. Examples of these include predators like African wild dogs, hyenas, wolves, Brown falcon, Harris's hawk, and some aquatic creatures like Sevengill sharks [12–18]. Using the hunting cooperation technique, predators get more advantages, such as a higher probability of capturing large preys, higher rates of success in hunting as a result of increasing the number of adults, the ability to find food more quickly, a reduction in the search for other species [15]. However, excessive hunting can be dangerous to predators and even result in its extinction.

In ecological systems, many predators usually dwell in groups and establish hunting cooperative strategies throughout a period. Such cooperative behavior increases the prey's chances of success, but it also makes them fearful of predators, which lowers their reproductive rate. The dynamic nature of the populations that interact is greatly influenced by the fear of prey in the presence of predators within the ecosystem. In addition to hunting directly, the predator can also have an indirect impact on prey though behavioral changes and stress-related adaptations. Furthermore, fear may affect their ability to survive as adults [19]. For instance,

the reproduction process of elks is influenced by wolves in the wider ecosystem of Yellowstone [20]. Based on this occurrence, a predator-fear element was introduced into the birth rate of prey by Wang et al. [21] which demonstrates that a high degree of fear could support the system. Many authors investigated the influence of fear in different forms, such as an exponential form of fear function [22] and a fear factor with a nonzero minimum cost of fear [23], etc.

In addition, every species has the potential to relocate for a variety of causes, including the availability of resources and turbulent diffusion. Therefore, it is more reasonable to include the geographical distribution of individuals in the mathematical modeling of the interaction between predators and prey [24,25]. To understand the spatio-temporal dynamics of system involving hunting cooperation and fear effect, reaction–diffusion systems are beneficial, as their solutions provide a good approximation of the dynamics. In reaction–diffusion systems, ecologists and mathematicians have recently paid a lot of attention to understanding the effects of self and cross diffusions. Alan Turing [26] introduced a dynamic process that combines chemical reactions with mathematical analysis. This mechanism explains that Turing instability, also known as diffusion-driven instability, occurs when the initially stable spatially uniform state of a system becomes unstable due to spatial diffusion. Therefore, vibrant spatial patterns emerge. Expanding upon the groundbreaking research of Turing [26], Segel and Jackson [27] were the first to apply Turing's notion to the study of bio-ecological models. Turing instability and pattern formation theory have found diverse and significant applications across various scientific and social disciplines. Recently, researchers have extended these concepts beyond classical ecological and chemical systems to complex human and information networks. For instance, in [28] the Turing instability is analyzed in rumor propagation systems on continuous and complex networks, revealing how spatial effects influence the spread of information. In [29] dynamic pattern formation and optimal control strategies are explored in rumor dynamics across different network structures, while in [30] generalized Turing pattern theory is applied to homogeneous and heterogeneous higher-order temporal networks, providing new insights into collective behaviors in interconnected systems. Moreover, [31] investigated spatio-temporal pattern dynamics in infectious disease models on complex networks. Additionally, [32] applied Turing pattern analysis to West Nile virus transmission on higher-order network topologies, highlighting the wide applicability of pattern formation theory in modeling real-world complex phenomena.

Several predators exhibit cooperative behavior when hunting and also instill fear in their prey. Wolves act as a possible essential specie by cooperating during hunting and exerting indirect effects on their prey [18]. The article [33] examined a predator–prey system that considered fear, hunting cooperation, and predator density-dependent mortality in the presence of self-diffusion. In a model, [34] examined cross-diffusion with hunting cooperation in predator–prey system. The spatio-temporal dynamics of a predator–prey model with generalist predator and effects of fear and hunting cooperation was analyzed in [35], and the dynamics of fear and behavior of hunting cooperation in a Leslie–Gower model in [36]. Motivated by these considerations, the present work focuses on the combined influence of fear and diffusion with an increasing type of functional response. Mathematically speaking, fear and spatial diffusion play a crucial role in determining the dynamic behavior of various differential systems. The inclusion of these mechanisms can lead to a range of dynamical consequences, including alterations in stability, the emergence of bifurcations, and the onset of complex spatio-temporal patterns. The fear of predation reduces prey reproduction, introducing a non-consumptive interaction. The inclusion of diffusion captures the spatial movement of species, leading to possible pattern formation and spatio-temporal oscillations. This framework provides insight into spatial heterogeneity, coexistence, and localized extinctions. It is relevant for ecological management, conservation, and understanding complex predator–prey interactions in natural habitats.

The structure of the current manuscript is described below. In Section 2, we present the model of the predator–prey system studied, which incorporates the fear induced by anti-predator actions with increasing type of functional response and studies the determination of positive equilibrium states of the system. In Section 3, we study the feasibility of the system, the nature of equilibrium states, and some bifurcations. We also analyze the influence on the basins of attraction resulting from the incorporation of fear modification into the model. In Section 4, the conditions of Turing instability and various types of patterns of the corresponding diffusive system are discussed. In Section 5, we conclude the article with a discussion.

2. Mathematical model

A predator–prey model proposed by Ryu et al. [37] incorporating the hunting cooperation type of functional response is given as follows:

$$\begin{cases} \dfrac{dN}{dT} = r_1 N - r_2 N^2 - \dfrac{a\, b_0 N P^2}{1 + h\, a\, b_0 N P}, \\ \dfrac{dP}{dT} = \dfrac{e\, a\, b_0 N P^2}{1 + h\, a\, b_0 N P} - d\, P, \\ N(0) \geq 0, \quad P(0) \geq 0. \end{cases} \tag{1}$$

The parameters r_1 and r_2 represent the intrinsic growth rate and the intra-specific competition coefficient of the prey population, respectively. The parameter a is the fraction of a prey species killed per predator per encounter and h is the handling time per prey. The constants e and d are the consumption rate of the captured prey by the predators and the natural mortality rate of predators.

Wang et al. [21] proposed a specific form of the fear effect term, $G(F, P) = \frac{1}{1+FP}$, applied to the growth rate of the prey population. The parameter F represents the level of fear that drives the prey to engage in anti-predator activities. Recently, many authors [21,38–40] have explored the effect of fear on prey populations as:

$$\frac{r_1 N - r_2 N^2}{1 + FP} = \frac{(r_1 + r_2) N \left(1 - \frac{r_2}{r_1 + r_2} N\right) + r_2 F N P}{1 + FP} - r_2 N,$$

where, first term of right side is combined reproduction of prey due to fear of predator and second term is natural death rate of prey population. Researchers of the articles [39–42] have investigated the impact of fear by incorporating fear functions into the entire logistic growth rate of the prey population. Zanette et al. [43] experimentally demonstrated that fear of predators can substantially reduce reproductive success in songbirds, reporting about a 40% decline in annual offspring production. Despite this reduction, reproduction was not completely halted, indicating adaptive behavioral adjustments rather than total reproductive suppression. Later on Elliott et al. [44] provided experimental evidence that predator-induced fear can diminish prey growth rates, further emphasizing the significant role of fear in shaping prey population dynamics. These findings underscore the critical role fear plays in shaping ecological interactions, prompting further exploration of its effects. Motivated by the aforementioned studies, we incorporate the fear factor into the entire logistic growth term of the prey population within the predator–prey model proposed by [37]. Consequently, the model (1) is extended as follows:

$$\begin{cases} \dfrac{dN}{dT} = \dfrac{r_1 N - r_2 N^2}{1+FP} - \dfrac{a\,b_0 N P^2}{1+h\,a\,b_0 N P}, \\ \dfrac{dP}{dT} = \dfrac{e\,a\,b_0 N P^2}{1+h\,a\,b_0 N P} - d\,P, \\ N(0) \geq 0, \quad P(0) \geq 0. \end{cases} \tag{2}$$

For ecological purposes, we examine the model (2) within the domain $\Gamma_1 = \{(N,P) \in \mathbb{R}^2, N \geq 0\ , P \geq 0\}$. To simplify the study, we adjust this model to a topologically identical non-dimensionalized model with a lesser number of parameters. For this reason, we implement a change of variables and time scaling, according to the functions

$$\Psi : \Gamma_1 \times \mathbb{R} \to \Gamma_2 \times \mathbb{R} \ \text{ defined as } \ \Psi(N,P,T) = (X,Y,t) \ \text{ with } \ X = \frac{r_2}{r_1} N, \quad Y = \frac{h\,a\,b_0 r_1}{r_2} P,$$

$$t = r_1 T, \quad \text{where } \ \Gamma_2 = \{(X,Y) \in \mathbb{R}^2, X \geq 0\ , Y \geq 0\} \ \text{ and } \ \tau = \frac{r_2^2}{a\,b_0 h^2 r_1^3},$$

$$\mu = \frac{e}{h\,r_1}, \quad \epsilon = \frac{d}{r_1}, \quad f = \frac{r_2 F}{h\,a\,b_0 r_1}.$$

Introducing these new parameters into system (2), we get the following equivalent form:

$$\begin{cases} \dfrac{dX}{dt} = \dfrac{X(1-X)}{1+fY} - \dfrac{\tau X Y^2}{1+XY} \equiv X f(X,Y), \\ \dfrac{dY}{dt} = \dfrac{\mu X Y^2}{1+XY} - \epsilon Y \equiv Y g(X,Y), \\ X(0) = X_0 \geq 0, \quad Y(0) = Y_0 \geq 0. \end{cases} \tag{3}$$

From now on, we will analyze the equivalent system (3) for mathematical simplicity. It should be noted that this article focuses on the theoretical study of the different possible dynamics and on understanding the effect of different parameters on the model. An interesting future extension is to link this model with data-driven techniques to provide a model tailored to specific realistic values, as has been done recently [45] with other models.

2.1. Number of equilibrium states

In this subsection, we examine the existence of all nonnegative equilibrium states of the system (3). The nullclines intersections of $\frac{X(1-X)}{1+fY} - \frac{\tau XY^2}{1+XY} = 0$ and $\frac{\mu XY^2}{1+XY} - \epsilon Y = 0$ provide the ecologically feasible equilibria in $\Gamma_2 = \{(X,Y) \in \mathbb{R}^2, X \geq 0\ , Y \geq 0\}$. The curve $f(X,Y) \equiv \frac{1-X}{1+fY} - \frac{\tau Y^2}{1+XY} = 0$ and $X = 0$ are the prey nullclines. Also, the predator nullclines are provided as $Y = 0$ and the curve $g(X,Y) \equiv \frac{\mu X}{1+XY} - \epsilon = 0$. The system (3) has a trivial equilibrium $E_0(0,0)$ and the predator-extinction equilibrium $E_k(1,0)$. The following two algebraic equations hold correct if the system exhibits a positive interior equilibrium:

$$\frac{1-X}{1+fY} = \frac{\tau Y^2}{1+XY} \quad \text{and} \quad \frac{\mu XY}{1+XY} = \epsilon.$$

That is, the interior equilibrium states $E_i^*(X_i, Y_i)$ are given by

$$p(X) \equiv X^4 - X^3 + \frac{\tau\epsilon^2}{\mu(\mu-\epsilon)} X + \frac{\tau f \epsilon^3}{\mu(\mu-\epsilon)^2} = 0 \tag{4a}$$

$$Y = \frac{\epsilon}{(\mu-\epsilon)X}, \tag{4b}$$

where X_i, represents the positive roots of quartic equation ((4)a) and $Y_i = \frac{\epsilon}{(\mu-\epsilon)X_i}$. We may find the positive roots of equation ((4)a) by applying Descartes' rule of sign. The coefficients of X^3 have negative sign and all other coefficients have positive sign when $\mu > \epsilon$. So, there is a possibility that Eq. (4)(a) will have zero or two positive roots. As a result, the system (3) has zero or two feasible interior equilibrium states which are represented by $E_1^*(X_1, Y_1)$ and $E_2^*(X_2, Y_2)$, where $X_1 < X_2$. If $\mu < \epsilon$ then there is no feasible interior equilibria. It is very challenging to determine the exact parametric constraints required for the possible co-existing

equilibrium state. However, examining every possible relative position of the two nullclines $f(X,Y)=0$ and $g(X,Y)=0$, we observe that effectively the number of interior equilibrium states of the system (3) varies from zero to two, depending on parameters. That is, the system always have the $E_0(0,0)$ and $E_k(1,0)$ equilibria in the axis, and in some parameter regions also the interior equilibria $E_1^*(X_1,Y_1)$ and $E_2^*(X_2,Y_2)$.

First, we proved some trivial results that simply state that the model is well designed from the real point of view (positive and bounded solutions).

Proposition 1. *The system (3) with initial conditions in the first quadrant of the XY-plane possesses a unique positive solution.*

Proof. The result is trivial as the X and Y axes are invariants of the system, and thus no orbit can cross them. Therefore, the solutions with initial conditions on the first quadrant are always positive. Uniqueness and existence are obtained directly as per the recent articles [46–48], since in this case the system is smooth enough to apply the classical existence theorems taking into account the positivity of the solutions. □

Theorem 1. *Each solution $(X(t),Y(t))$ of the system (3) with initial conditions (X_0, Y_0) inside the polygonal region*

$$S=\left\{(X,Y):0\le X\le L_1,\ 0\le Y\le\left\{0,\ \frac{\mu}{\tau\epsilon}\left(L_2-\epsilon X\right)\right\}\right\},$$

where $L_1=\max(1,X_0)$ and $L_2=\frac{(1+\epsilon)^2}{4}$, remains in S. That is, S is a trapping region for the dynamics of the system.

Proof. The first part (lower bound, $X,Y\ge 0$) is trivial as the X and Y axis are invariants of the system (Proposition 1), and so no orbit can cross them.

The boundedness proof of this theorem is done on the similar lines as discussed in the article [37] by using integration and Gronwall's inequality [49]. If we integrate the equations of system (3) in the interval $[0,t]$, we trivially get

$$X(t)=X_0\exp\left(\int_0^t f(X(u),Y(u))du\right),\quad Y(t)=Y_0\exp\left(\int_0^t g(X(u),Y(u))du\right). \tag{5}$$

Firstly, we show the bound on $X(t)$ and then we proof it for $Y(t)$. Here, we consider two cases, depending on the initial value of the prey population: (i) $X_0\le 1$ and (ii) $X_0>1$. In the first case, we assert that for any $t>0$, $X(t)\le 1$. In contrast, we suppose that there exist positive t_0, t_1 such that $t_0<t_1$ and $X(t_0)=1$ where $X(t)>1$ for $t\in(t_0,t_1)$. For $T_0\in(t_0,t_1)$, utilizing Eq. (5), we get

$$X(T_0)=X_0\exp\left(\int_0^{t_0} f(X(u),Y(u))du\right)\exp\left(\int_{t_0}^{T_0} f(X(u),Y(u))du\right),$$

$$=X(t_0)\exp\left(\int_{t_0}^{T_0} f(X(u),Y(u))du\right)\le X(t_0).$$

This is valid because $f(X(u),Y(u))<0$ for $t\in(t_0,t_1)$ and contradicts the statement $X(t)>1$. So, we have $X(t)\le 1$ for any $t>0$ in this instance. Now, if $X_0>1$ then there are two possible sub-cases: either $X(t)>1$ for $t>0$ or there exists $T_1>0$ such that $X(t)>1$ for given $t\in[0,T_1)$ with $X(T_1)=1$. In the second sub-case, $X(t)\le 1$ for all $t>T_1$ and for contradicting assumptions $t\in(0,T_1)$, we obtain

$$X(t)=X_0\exp\left(\int_0^t f(X(u),Y(u))du\right)\le X_0.$$

By similar analysis, we can demonstrate that $X(t)\le X_0$ in the first sub-case. Hence, we summarize above result as $X(t)\le\max(1,X_0)$. Now, to show the boundedness of $Y(t)$, we proposed a function $U(t)=X(t)+\frac{\tau}{\mu}Y(t)$, to get

$$\frac{dU(t)}{dt}+\epsilon U(t)=\frac{X}{1+fY}(1-X)+\epsilon X.$$

Since, the prey population density decreases by fear effect of predator, so, we get

$$\frac{dU(t)}{dt}+\epsilon U(t)\le X(1+\epsilon-X),$$

The maximum value of the function $X(1+\epsilon-X)$ is L_2, which is obtained at the critical point $X=\frac{1+\epsilon}{2}$, then

$$\frac{dU(t)}{dt}+\epsilon U(t)\le L_2.$$

Now, using Gronwall's inequality described in [49], we obtain,

$$\limsup_{t\to\infty}\left(X(t)+\frac{\tau}{\mu}Y(t)\right)\le\frac{L_2}{\epsilon},$$

which shows that any solutions of (3) that originates from the region S will be confined in it. In ecology, bounded solutions mean that no any species rapid or exponential growth over time rather they have a restricted population density due to limited resources. □

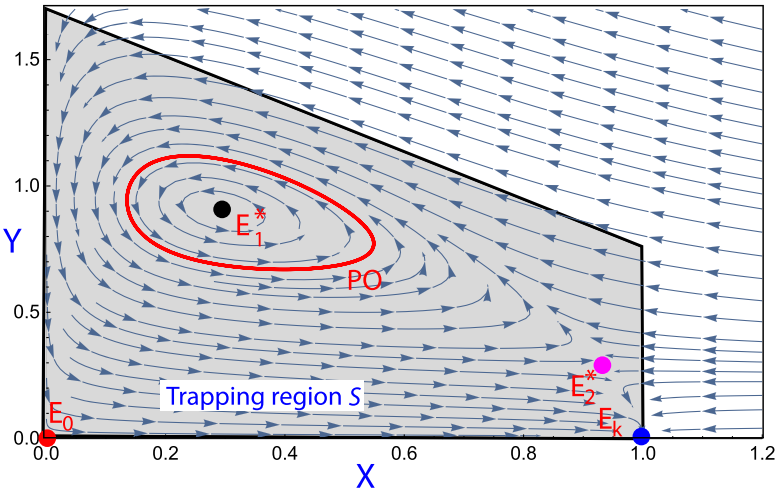

Fig. 2. Example of the phase space and the trapping region S (for $X_0 = 1$).

Note that the global boundedness is easily obtained since when $X > 1$ then always $dX/dt < 0$ and when Y is large then also $dX/dt < 0$ regardless of X, i.e. for large Y, X decreases, and when X is small $dY/dt < 0$, and therefore, the orbits for large values of X_0 or Y_0 reach a maximum and then decrease entering the S region. In fact, it is clear that outside S the dynamics is trivial, and in S all equilibria and periodic orbits are placed. That is, S attracts all the dynamics. Therefore, we can state

Corollary 1. *The trapping region S is a globally attracting region for the dynamics of the system (3).*

As illustration, in Fig. 2, we plot for $f = 0.1$, $\tau = 1$, $\mu = 0.95$ and $\epsilon = 0.2$ the phase space, with the equilibria and the periodic orbit that coexist in this case, and the trapping (and globally attracting) region with $X_0 = 1$.

Positivity implies that the population densities of both prey and predator remain non-negative for all time and space. This reflects the biological fact that negative population sizes are meaningless; that is, species cannot exist in negative quantities. Therefore, positivity guarantees that the model describes physically and ecologically feasible population levels throughout the ecosystem. Boundedness indicates that the populations do not grow without limit but remain within a finite range determined by environmental constraints such as limited food resources, habitat capacity, and natural mortality. This reflects the ecological principle of carrying capacity, ensuring that neither species can explode to infinity, which would be ecologically impossible.

3. Main results

In this section, we perform the stability and bifurcation analysis of all feasible equilibrium states of system (3).

3.1. Nature of the equilibrium states

Here, we mainly analyze the nature of equilibrium states in term of local and global asymptotic stability of the system (3). The stability behaviors of positive state may not always be analytically determined. In such cases, we use numerical and graphical approach to explain such features. For this purpose, we calculate the following linearized matrix J of the system at any general equilibrium state $E(X, Y)$:

$$J_{E(X,Y)} = \begin{pmatrix} \frac{1-2X}{1+fY} - \frac{\tau Y^2}{(1+XY)^2} & \frac{-X(1-X)f}{(1+fY)^2} - \frac{\tau XY(2+XY)}{(1+XY)^2} \\ \frac{\mu Y^2}{(1+XY)^2} & \frac{\mu XY(2+XY)}{(1+XY)^2} - \epsilon \end{pmatrix}. \tag{6}$$

The linearized matrix at $E_0(0,0)$ is $J_{E_0} = \begin{pmatrix} 1 & 0 \\ 0 & -\epsilon \end{pmatrix}$. Obviously, J_{E_0} has two characteristic roots $1, -\epsilon$, so $E_0(0,0)$ is always a saddle point. The linearized matrix J at $E_k(1,0)$ is $J_{E_k} = \begin{pmatrix} -1 & 0 \\ 0 & -\epsilon \end{pmatrix}$. The matrix J_{E_k} has two characteristic roots -1 and $-\epsilon$ that are negative, so the equilibrium state $E_k(1,0)$ is always an attractor node.

From Theorem 1, we have that solutions originating in the positive quadrant of the XY-plane are bounded and ultimately finish in the S region. Additionally, as the equilibrium state $E_0(0,0)$ is a saddle point, and when E_1^* and E_2^* equilibria are no present (and so there are no equilibrium in the interior of the first quadrant), then, according to the Poincare–Bendixson theorem [50] the equilibrium state $E_k(1,0)$ is the unique ω-limit of any trajectory. Therefore, in this situation the point $E_k(1,0)$ is globally asymptotically stable (see an illustration in Fig. 6(d)).

Now, we study briefly the interior equilibria $E_i^*(X_i, Y_i)$. The characteristic polynomial of the linearized matrix of system (3) evaluated at the co-existing equilibrium states $E_i^*(X_i, Y_i)$, for $i = 1, 2$ is given by $\lambda^2 - Tr(J_{E_i^*})\lambda + \det(J_{E_i^*})$ where

$$Tr(J_{E_i^*}) = \frac{\epsilon+\mu}{\mu}\left[\frac{\epsilon}{\epsilon+\mu}\left(\frac{1}{1+fY_i}+\mu-\epsilon\right) - \frac{X_i}{1+fY_i}\right] \quad \text{and}$$

$$\det(J_{E_i^*}) = \frac{\epsilon(\mu-\epsilon)}{\mu(1+fY_i)X_i^3}\left(2X_i^3 - 3X_i^4 + \frac{f\tau\epsilon^3}{\mu(\mu-\epsilon)^2}\right).$$

Here, $Tr(J_{E_i^*})$ and $\det(J_{E_i^*})$ represent the trace and determinant of linearized matrix at state (X_i, Y_i), respectively. According to the stability criterion [51], two roots with a negative real component must satisfy the criteria of $Tr(J_{E_i^*}) < 0$ and $\det(J_{E_i^*}) > 0$. It is difficult to find explicit expressions for the interior equilibrium states, and as a result the study of the stability of these states analytically becomes considerably more challenging. Therefore, we examine the stability of the coexisting equilibrium states using the graphical Jacobian method and the overall nature of the two nullclines with respect to the direction of their vector fields. By examining the vector fields in several parametric planes, one can easily determine that E_2^* (when it exists) is a saddle point in all studied cases. If E_1^* is present, it can experience both stability and instability. For example, if we consider the set of parameters $\tau = 1$, $\mu = 0.95$, $\epsilon = 0.2$, $f = 0.95$, we observe that E_1^* is stable and E_2^* is a saddle point. On the other hand, if we take the parameter set $\tau = 1$, $\mu = 0.95$, $\epsilon = 0.2$, $f = 0.9$, then E_1^* is unstable and E_2^* remains a saddle point.

3.2. Local bifurcation analysis

In this subsection, we use bifurcation continuation techniques to show numerically that system (3) experiences some local bifurcations including Hopf, saddle–node, and Bogdanov–Takens. Sotomayor's theorem [50] and basic bifurcation theory presented in [52] can be used to prove the presence of these local bifurcations and their non-degeneracy once fixed the parameters of the system. All the continuation results have been obtained using the MATCONT software [53].

Oscillatory patterns, often seen in population dynamics, suggest intricate dynamics within ecological systems. The presence of oscillations or the appearance of a limit cycle generally signifies a Hopf bifurcation in the system [52]. A local change in the stability characteristics of an equilibrium state causes a periodic orbit to emerge or vanish, which is known as the Hopf bifurcation. Since, for the Hopf bifurcation, the analytical expression for X_1 and Y_1 is not available, we calculate the threshold values $f_{[H]}$ and $\tau_{[H]}$ numerically for some examples. For the first set of parameters ($\tau = 1$, $\mu = 0.95$, $\epsilon = 0.2$), we obtain $f_{[H]} = 0.9316$. For other set of parameters ($f = 0.8$, $\mu = 0.95$, $\epsilon = 0.1$), we obtain $\tau_{[H]} = 1.982667$. For both parameter sets, the equilibrium point E_1^* loses its stability through a Hopf bifurcation. Since both an interior equilibrium and an axial equilibrium remain stable between the Hopf bifurcation (H) and the saddle–node bifurcation (SN), this defines a bistable region between these two bifurcations [see Fig. 3]. Note that due to the Hopf bifurcation the bistability is between two stable equilibria or one stable equilibria and on stable limit cycle. The proposed system experiences supercritical and subcritical Hopf bifurcation [52] if the first Lyapunov coefficient is $L_1 < 0$ or $L_1 > 0$, respectively. Due to the complexity of the first Lyapunov coefficient formula as well as the unavailability of the explicit expression of the co-existing equilibrium state, we are unable to determine the sign of L_1 analytically. However, in all our numerically studied cases we have found a supercritical Hopf bifurcation for the model (3).

As illustration of the existence of the Hopf bifurcation we show two numerical examples. If we take the set of parameters $\tau = 1$, $\mu = 0.95$, $\epsilon = 0.2$ and f passes through $f_{[H]} = 0.9316$ then the co-existing equilibrium state $E_1^*(0.3878865410, 0.6874862582)$ change its stability and $E_2^*(0.9146710194, 0.2915438021)$ remains saddle and which corresponding eigenvalues are $\lambda_{1,2} = \pm 0.3217i$ and $\lambda_1 = -0.6798$, $\lambda_2 = 0.1325$, respectively. Thus, the system (3) experiences a Hopf bifurcation (Fig. 3) leading to the appearance of a stable periodic cycle, as shown in Fig. 4(a). For these values of parameters, the first Lyapunov coefficient is $L_1 = -0.3404679168 < 0$, and therefore the Hopf bifurcation is supercritical.

On the other hand, if we choose another set of parameters $f = 0.8$, $\mu = 0.95$, $\epsilon = 0.1$ and $\tau = \tau_{[H]} = 1.982667$, then the interior equilibrium state $E_2^*(0.9714625476, 0.1211030308)$ is saddle and $E_1^*(0.2121106289, 0.5546495216)$ switch its stability through a supercritical Hopf bifurcation (first Lyapunov coefficient $L_1 = -0.3068676807 < 0$ and $\det[J_{E_1^*}] = 0.0995$), and as a result a stable periodic cycle appears. This process is illustrated in Figs. 4(b) and 5. At this parametric set, $\lambda_{1,2} = \pm 0.3154i$ and $\lambda_1 = -0.8781$, $\lambda_2 = 0.0847$ are the eigenvalues of E_1^* and E_2^*, respectively. Thus, the system (3) possesses a supercritical Hopf bifurcation for both sets of studied parameter values and its corresponding bifurcation diagram are shown in Fig. 4.

We have observed that the co-existing interior equilibrium state E_1^* is locally asymptotically stable or unstable and E_2^* is always saddle (in the studied cases). These two equilibrium states overlap with each other and give rise to a unique state $\bar{E}_{SN}(X_0, Y_0)$ when the parameter ϵ changes in a small neighborhood of $\epsilon_{[SN]}$. Analytical conditions for saddle–node bifurcation are difficult to find for this system since we cannot find the explicit expression of the interior equilibrium states. To illustrate this bifurcation we show numerically with one example that the system (3) undergoes a saddle–node bifurcation at instantaneous equilibrium state $\bar{E}_{SN}(X_0, Y_0)$. Given the set of parameters $f = 0.9$, $\tau = 1$ and $\mu = 0.95$, we get a threshold value $\epsilon_{[SN]} = 0.256282769$, where $\mathrm{Det}[J_{\bar{E}_{SN}}] = 0$. The proposed system shows a saddle–node bifurcation in neighborhood of equilibrium state $\bar{E}_{SN}(0.6990071205, 0.5285125762)$ at this threshold value $\epsilon_{[SN]}$. The system has no interior equilibrium state when parameter ϵ is greater than $\epsilon_{[SN]}$. As a result of this situation all trajectories go to the boundary equilibrium state $E_k(1, 0)$. Ecologically, we can say that the prey population reaches its maximum threshold value and the population of predator may go to extinction. When $\epsilon < \epsilon_{[SN]}$, then the system generates two interior equilibrium state which one of them is a saddle point and another one changes its stability through a Hopf bifurcation, which is already discussed in above subsection.

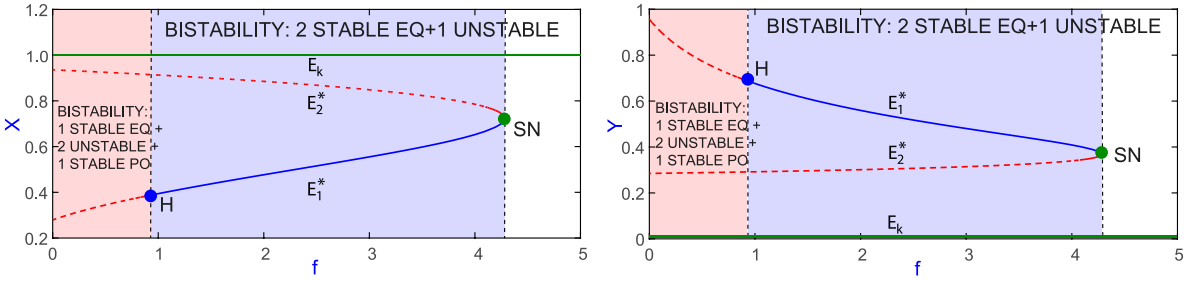

Fig. 3. Panel (a) and (b) present the bifurcation diagram with respect to f with on the density of X and Y population, respectively showing the supercritical Hopf (H) and saddle–node (SN) bifurcation points. We plot the branches of the E_1^* and the unstable E_2^* interior equilibria (the continuous blue and discontinuous red curves denote stable and unstable branches respectively). The green curve represents the stable axial equilibrium $E_k(1,0)$. The bistability region is remarked in cases of two stable equilibria or one stable equilibrium plus one stable periodic orbit. (For interpretation of the references to color in this figure legend, the reader is referred to the web version of this article.)

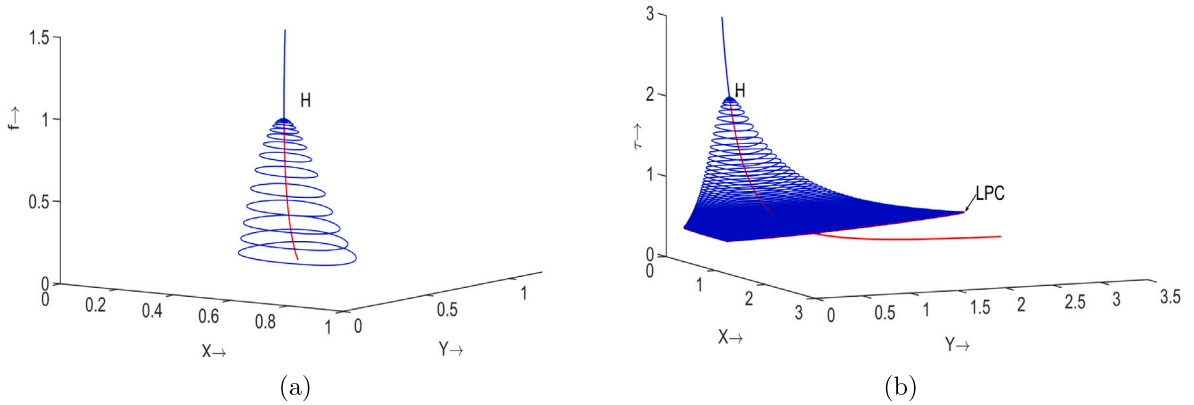

Fig. 4. Figures (a)(case of Fig. 3) and (b)(case of Fig. 5) illustrate the stable limit cycles created at a supercritical Hopf bifurcation with respect to fear parameter f and τ.

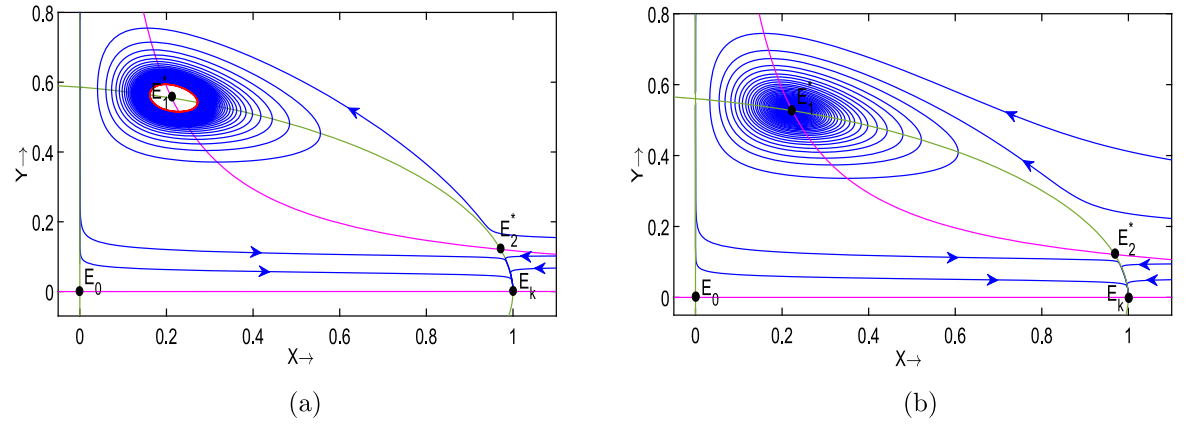

Fig. 5. Phase diagram of the system (3) for two values of the parameter τ. In (a) a stable periodic limit cycles originated at a Hopf bifurcation around E_1^* unstable equilibrium), for $\tau_{[H]} = 1.982667$, and (b) showing that E_1^* is stable for $\tau \equiv 2.2 > \tau_{[H]}$. The green and purple lines describe the nullclines. Here, the interior equilibrium E_2^* is always a saddle point. (For interpretation of the references to color in this figure legend, the reader is referred to the web version of this article.)

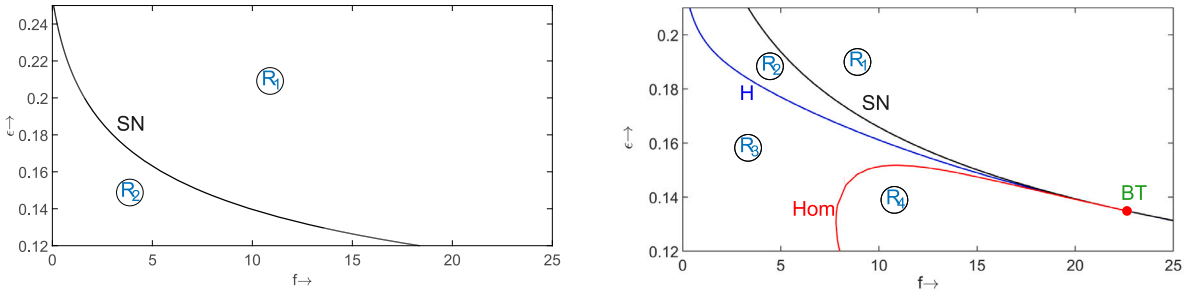

Fig. 6. Biparametric bifurcation diagram in (f, ϵ)- plane. BT represents Bogdanov–Takens point; SN (black curve), H (blue curve) and Hom (red curve) represents saddle–node, Hopf and homoclinic bifurcation curves, respectively, (a) for $\tau = 1$, $\mu = 0.8$, (b) $\tau = 1$, $\mu = 0.95$. (For interpretation of the references to color in this figure legend, the reader is referred to the web version of this article.)

Table 1
Dynamical behavior of the equilibrium states in each region for the system (3). Trivial equilibrium state E_0 is always unstable in all regions.

Region (phase dynamics)	E_k	E_1^*	E_2^*	Remarks
R_1 (Fig. 9(a))	Stable	–	–	Axial equilibrium E_k is globally asymptotically stable.
At BT-point (Fig. 9(b))	Stable	–	–	E_1^* and E_2^* collide and give rise a degenerate equilibrium state $\bar{E}$.
R_2 (Fig. 9(c))	Stable	Stable	Saddle	–
R_3 (Fig. 9(d))	Stable	Unstable	Saddle	E_1^* is encircled by an stable periodic cycle.
At homoclinic curve (Fig. 9(e))	Stable	Unstable	Saddle	A homoclinic cycle emerges around E_1^*.
R_4 (Fig. 6(f))	Stable	Unstable	Saddle	Axial equilibrium E_k is globally asymptotically stable.

When we plot the saddle–node and Hopf bifurcation curve in the (f, ϵ)-plane, the intersection of these two curves gives rise to another local bifurcation of co-dimension two [50,52]. This bifurcation is referred as the Bogdanov–Takens (BT) bifurcation. Clearly, if both $p(X) = 0$ (Eq. (4)) and $p'(X) = 0$ are satisfied simultaneously, then two positive equilibria, $E_1^*(X_1, Y_1)$ and $E_2^*(X_2, Y_2)$ coincide each other and give rise to a degenerate equilibrium $\bar{E}(X_0, Y_0)$. It is easy to verify that the linearized matrix at $\bar{E}$ has a zero eigenvalue of multiplicity two when $\det(J_{\bar{E}}) = Tr(J_{\bar{E}}) = 0$. We choose f and ϵ as the bifurcation parameters because they are significant from an ecological perspective. A threshold pair $(f_{[BT]}, \epsilon_{[BT]})$ can be determined from $\det(J_{\bar{E}})|_{(f_{[BT]}, \epsilon_{[BT]})} = 0$ and $Tr(J_{\bar{E}})|_{(f_{[BT]}, \epsilon_{[BT]})} = 0$ while maintaining the other parameters fixed. It is observed that finding explicit expressions for f and ϵ is challenging so, we illustrate numerically this result. For the set of parameters $\tau = 1$, $\mu = 0.95$ the proposed system (3) undergoes Bogdanov–Takens (BT) bifurcation around the state $\bar{E}(X_0, Y_0) = (0.7392608591, 0.2237461422)$ at the pair of threshold value $(f_{[BT]}, \epsilon_{[BT]}) = (22.658623, 0.134834)$ and the corresponding parametric diagram for BT bifurcation with the help of MATCONT software [53] is shown in Fig. 6(b).

Additionally, the proposed system has only a saddle–node bifurcation when $\tau = 1$, $\mu = 0.8$ and there is no major bifurcations [see Fig. 6(a)]. As we increase the value of $\mu = 0.95$ then the system have regions with qualitatively distinct dynamics. Fig. 6(b) shows that there is no interior equilibrium state exists when (f, ϵ) lies in region R_1, so the axial state $E_k(1, 0)$ is globally asymptotically stable in this region. Ecologically, only prey population survive in the region R_1 and their population grow and attains its maximum threshold value. A saddle–node bifurcation arises when the pair of threshold value (f, ϵ) lies on the black curve. The proposed system (3) generates two interior equilibrium states when (f, ϵ) crosses to region R_2 via SN-curve, one of them is locally stable and the other is a saddle point. In other words, the predator and prey interact to each other and sustain their own density in the ecosystem. When the parameters (f, ϵ) cross the curve H into region R_3 a stable periodic cycle will arises through a supercritical Hopf bifurcation. A homoclinic cycle emerges when both, saddle–node and Hopf bifurcations occur simultaneously for the same equilibrium point $\bar{E}$ (a Bogdanov–Takens (BT) bifurcation point). It is known that at this BT point a homoclinic and a Hopf bifurcation curve are generated. Notably, the homoclinic bifurcation eliminates the periodic cycle generated at the Hopf bifurcation, giving a sudden change in the dynamics of the system. We will discuss this effect with more detail later. Besides, ecologically, prey and predator may coexist and their density may be more effectively maintained in the neighborhood of a homoclinic loop due to the slow rate of change. Finally, the system (3) displays a hyperbolic saddle point and an unstable focus when the parameters (f, ϵ) cross the homoclinic curve and enter in the region R_4. The dynamics of each region is listed in Table 1.

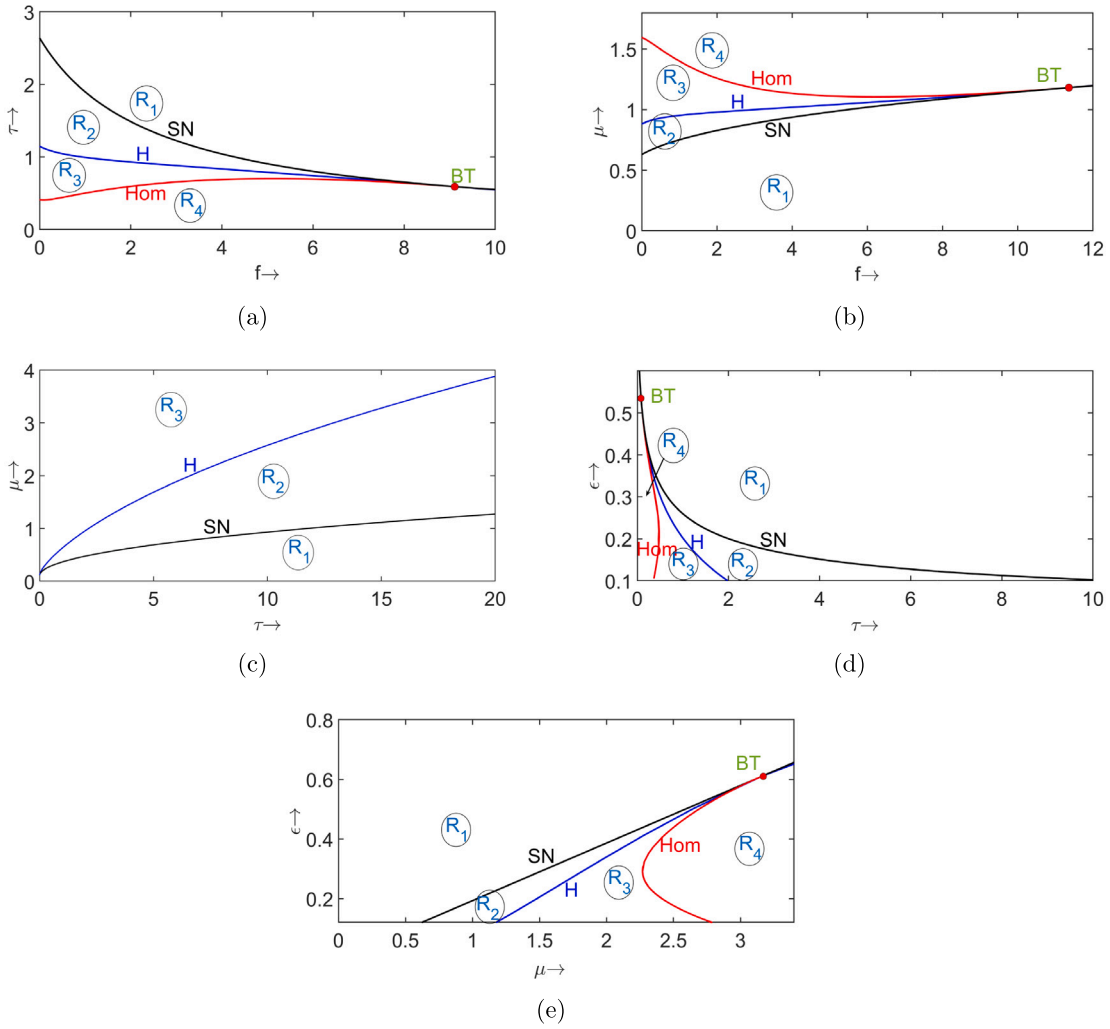

Fig. 7. Continuation bifurcation plots in (f, τ), (f, μ)-parametric planes for (a) $\mu = 0.95$, $\epsilon = 0.2$, (b) $\tau = 1$, $\epsilon = 0.2$. Bifurcation plot in (τ, μ), (τ, ϵ) and (μ, ϵ)-parametric planes for (c) $f = 0.8$, $\epsilon = 0.1$, (d) $f = 0.8$, $\mu = 0.95$ and (e) $f = 0.8$, $\tau = 2.5$.

The bifurcation scenario of the system (3) shown in Fig. 6(b) provides a global study in the biparametric plane (f, ϵ). But, what about the rest of parameters? In Fig. 7 we show the biparametric bifurcation results with respect to several pairs of parameters (the continuation results have been obtained with the software MATCONT [53]).

We analyze the dynamics of this system by changing fear parameter f with one of these parameters τ and μ respectively. The global picture is very similar to Fig. 6(b). The Hopf bifurcation curve separates the R_2 region and R_3 regions, while the homoclinic the R_3 region and R_4 regions. Regions R_1 and R_2 are separated by the saddle–node bifurcation curve. There are no interior equilibrium states in the R_1 region. However, when we move from region R_1 to R_2 then two co-existing equilibrium states E_1^* and E_2^* arise via the saddle–node bifurcation curve. Similarly, if we go from area R_2 to R_3 region, the number of interior equilibrium states remains the same, but the stability of equilibrium state E_1^* alters through Hopf bifurcation. From $f\tau$, $f\mu$-parametric bifurcations, we can demonstrate that rise in the level of fear destabilizes the proposed system and leads to the extinction of predator population or both populations [see Figs. 7(a)(b)].

We also discuss the dynamics of the proposed system by varying τ and together with one of the parameters μ and ϵ. The R_1 and R_2 areas are separated by a saddle–node bifurcation (SNB) curve. Similarly, the Hopf bifurcation (HB) curve separates the R_2 and R_3 regions. The classification and behavior of co-existing equilibrium states in all regions is the same as discussed above. From $\tau\mu$-parametric bifurcation [see Fig. 7(c)], we can conclude that the stability grows together with increase in the value of τ. However, if we increase the natural death rate (ϵ) of predator then system change stability and predator population may face as extinction [see Fig. 7(d)]. The stability region of the proposed system decreases by increasing the both parameters μ and ϵ, as a result the system destabilizes and predator or both populations may eventually become extinct [see Fig. 7(e)].

From Fig. 6, we observed that the bifurcation pattern was similar across all biparametric graphs, so our study was fairly generic and in the following we continued with the selected parameters as they were more biologically significant.

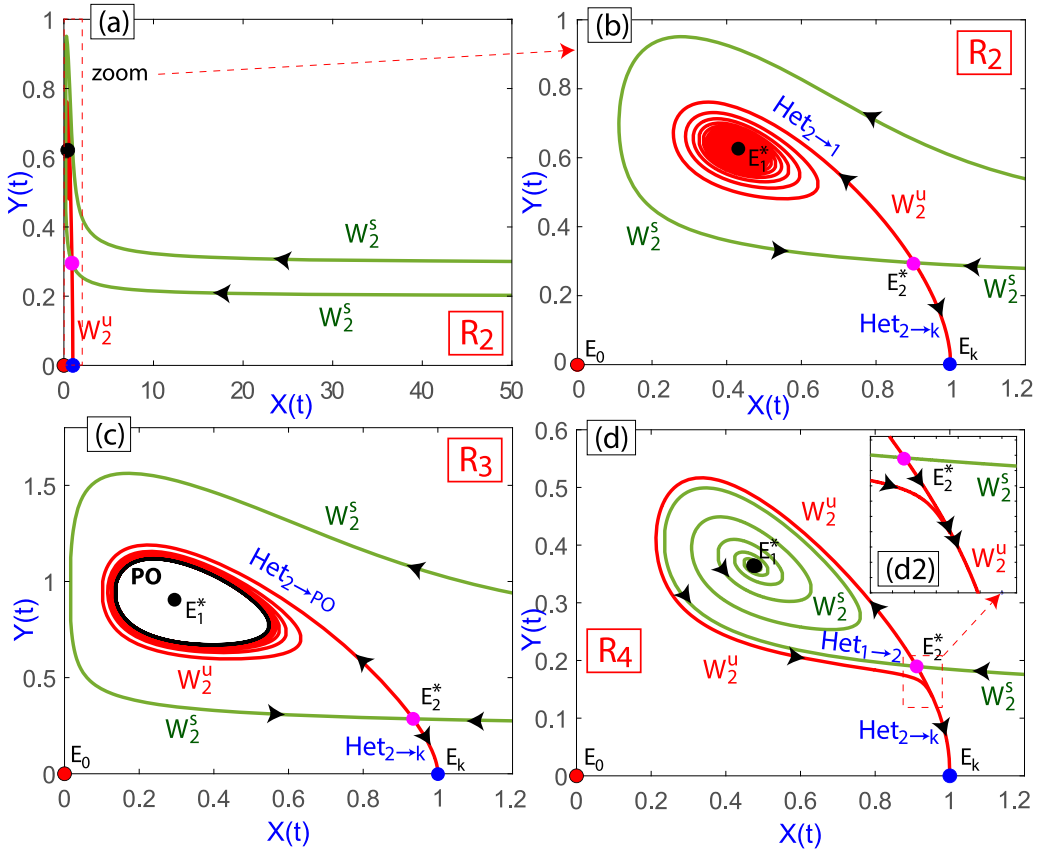

Fig. 8. Stable W_2^s and unstable W_2^u manifolds of E_2^* in the regions R_2 (plots (a) and (b)), R_3 (plot (c)) and R_4 (plot (d)). In some cases there are several heteroclinic connections (Het) between equilibria or an equilibrium and a stable periodic orbit.

3.3. Basins of attraction

In the previous subsection, we showed the basic bifurcations involved in describing the model's dynamics. In some cases, there is bistable behavior (regions R_2 and R_3), so describing the basins of attraction is key to showing the sets of initial conditions that lead to one or another dynamics. But, to that goal the study of the invariant manifolds of the saddle points is relevant. The equilibrium $E_0(0,0)$ is quite trivial as its stable and unstable manifolds are the coordinate axes, and so they provide no extra information. But the equilibrium E_2^* is an interior saddle point which stable manifold forms the separatrix among the different basins of attraction. In Fig. 8, we show in the regions R_2, R_3 and R_4 the stable W_2^s and unstable W_2^u manifolds of E_2^*. In region R_1, the dynamics is quite simple as there are just two equilibria, $E_0(0,0)$ and $E_k(1,0)$ and so no extra description is needed. In region R_2, we have from the study of previous sections, two stable equilibria. In Fig. 8(a), we show that W_2^s creates a large region that gives the basin of attraction of E_2^* that seems to continue in the X-axis. The rest of the plane converges to $E_k(1,0)$. In plot (b), we present a magnification in the region of interest showing the detailed structure of the manifolds. We also see that there are two heteroclinic connections, one from E_2^* to $E_k(1,0)$ ($\mathtt{Het}_{2\to k}$), and another from E_2^* to E_1^* ($\mathtt{Het}_{2\to 1}$). In region R_3 (plot (c)), we have after the Hopf bifurcation, one stable equilibrium and a stable limit cycle that takes the role of E_1^*. So we have two heteroclinic connections, one from E_2^* to $E_k(1,0)$ ($\mathtt{Het}_{2\to k}$), and another one from E_2^* to the stable periodic orbit (PO) ($\mathtt{Het}_{2\to PO}$). But on region R_4, there is a sudden change from the R_3 region as the PO collides with E_2^* giving a homoclinic orbit and so a homoclinic global bifurcation. The dynamics changes completely as now all the orbits converges to $E_k(1,0)$. The difference with R_1 is that this happens suddenly eliminating the stable periodic orbits in an abrupt way and not in a continuous case as in the change from R_2 to R_1. Therefore, this bifurcation is crucial as generates an important change of the dynamics without expecting it. Note that, in plot Fig. 8(d), the connections of the manifolds are different. We have a heteroclinic connection from E_1^* to E_1^* ($\mathtt{Het}_{1\to 2}$) reorganizing the stable manifold W_2^s that now does not create any basin of attraction.

Finally, in Fig. 9 we present the phase space configurations and the different basins of attraction in all regions and at the saddle–node and homoclinic bifurcations. The fixed parameters (unless indicated) are $\tau = 1$, $\mu = 0.95$ and $\epsilon = 0.2$. The golden region represents the basin of attraction the equilibrium state $E_k(1,0)$, the grey region shows the basin of attraction of the stable periodic cycle and the blue region shows the basin of attraction of the coexisting equilibrium state E_1^*, when they exist. The coexisting

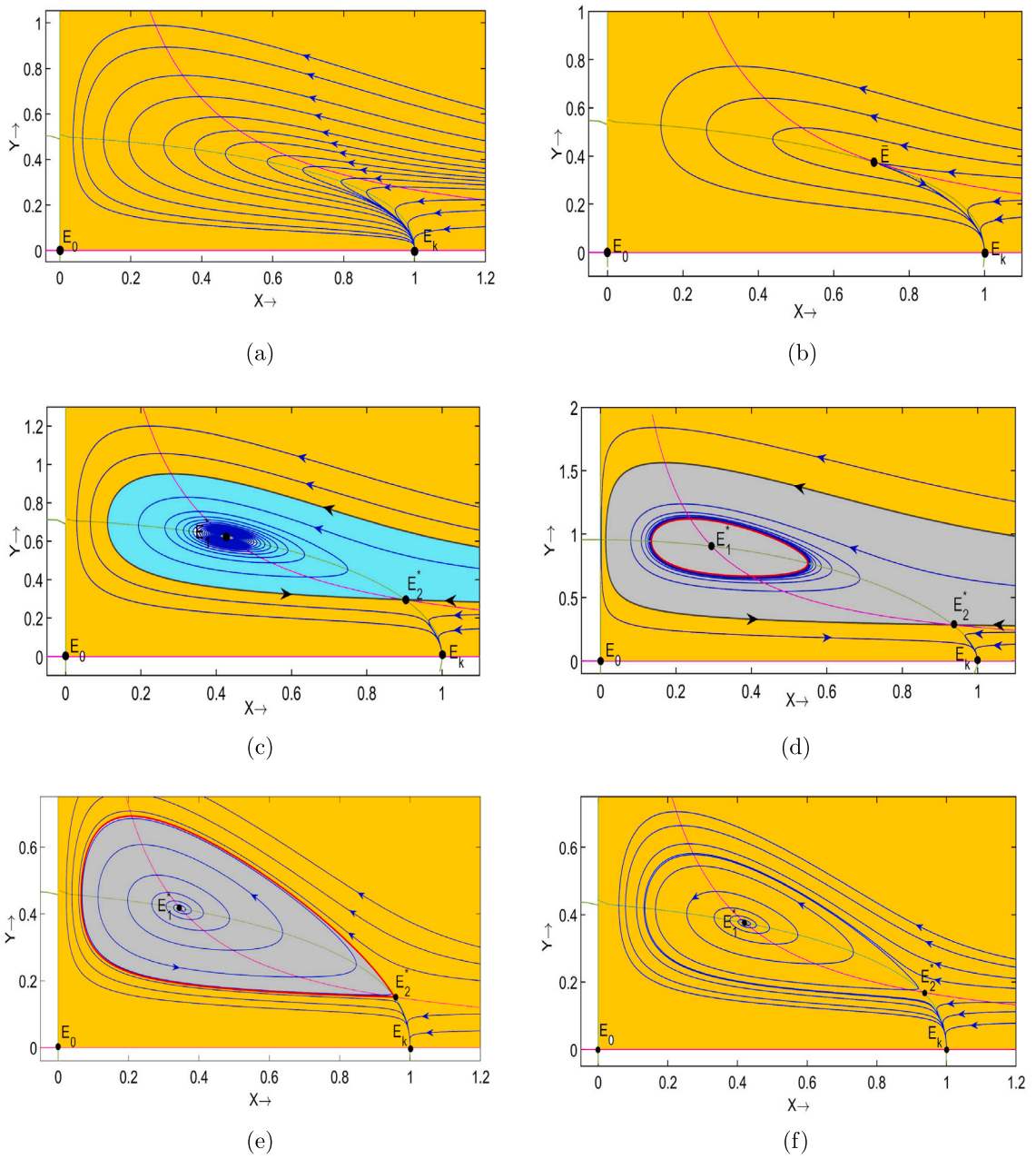

Fig. 9. Phase space dynamics and basins of attraction in the different regions and at the BT and homoclinic bifurcations. (a) global stability of E_k when no interior state exists (region R_1), (b) at BT-point $(f_{[BT]}, \epsilon_{[BT]}) = (22.658623, 0.134834)$, (c) $f = 1.4$, the equilibrium state E_1^* is stable (region R_2), (d) a stable periodic cycle around the equilibrium state E_1^* at $f = 0.1$ (region R_3), (e) Homoclinic cycle that emerges at $f = 0.8003891$, $\epsilon = 0.12$ and (d) both interior equilibrium state unstable as result $E_k(1,0)$ becomes global asymptotic stable (region R_4). $W^s(E_2^*) \equiv W_2^s$ forms the separatrix curve. The fixed parameters (unless indicated) are $\tau = 1$, $\mu = 0.95$ and $\epsilon = 0.2$.

equilibrium states collide at $\bar{E}(X, Y) = (0.7231624147, 0.3687507277)$ for $f_{[SN]} = 4.28154686$ and disappear for $f > f_{[SN]}$. So, now all trajectories initiating from the interior of the first quadrant attract towards predator-free state $E_k(1, 0)$. Hence, the extinction of the predator and prey logistically growth of prey population is observed in this case [see Fig. 9(d)]. Moreover, a greater fear impact on the prey population caused by the predator population is not beneficial to the predator population from an ecological perspective. A similar behavior is observed after the homoclinic bifurcation (region R_4), but as above commented, this happens suddenly.

In order to finish the study of the ODE model, we note that in [37] similar bifurcations were found for the model (1), but here the homoclinic bifurcation is detected providing a critical bifurcation in the model (3) (and so also in the model (2)) not detected previously. At this point it is interesting to remark that the use of control techniques may permit to ensure ecosystem balance as shown in [54] where two controls where introduced, one into the interspecific competition among prey, which results in a reduction

in biomass for both species and another one that uses an external food supply to the predators that depends upon the strong and weak preys (their model has two preys and one predator). Another interesting point of view is the use of optimal control and data-driven techniques [45] to achieve parameter identification based on realistic values.

4. Model with diffusion

The spatio-temporal predator–prey model have performed a crucial role in population development due to the significance of spatial patterns. Individuals often move randomly through space. Pattern formation may correctly depict population distributions throughout time and space. Spatial patterns can provide insights into individual development and the influence of mobility on other species, including stable and oscillatory behavior. The random migration of individuals from a higher density zone to a lower density zone is referred to as spatial self-diffusion. In the presence of self-diffusion the system (3) is modified as:

$$\begin{cases} \dfrac{\partial X}{\partial t} = \dfrac{X}{1+fY}(1-X) - \dfrac{\tau XY^2}{1+XY} + d_{11}\nabla^2 X, \\ \dfrac{\partial Y}{\partial t} = \dfrac{\mu XY^2}{1+XY} - \epsilon Y + d_{22}\nabla^2 Y, \end{cases} \tag{7}$$

where $d_{11} > 0$, $d_{22} > 0$ are the self-diffusion coefficients for prey and predator, respectively, and $\nabla^2 = \frac{\partial^2}{\partial x^2} + \frac{\partial^2}{\partial y^2}$ represents the usual Laplace operator. Self-diffusion terms in population of predator and prey represent the random movement of individuals. However, the population migration of a species in a given territory cannot be random. But movements of predator population also has an impact on the mobility of the prey population, and vice versa. We examine the system (7) with the following positive initial and zero-flux boundary conditions.

$$X(\vec{\omega},0) = X_0(\vec{\omega}) \geq 0, \quad Y(\vec{\omega},0) = Y_0(\vec{\omega}) \geq 0, \quad \vec{\omega} = (x,y) \in \Omega, \qquad t > 0 \tag{8}$$

with

$$\frac{\partial X}{\partial \vec{n}} = \frac{\partial Y}{\partial \vec{n}} = 0, \qquad (x,y) \in \partial\Omega, \qquad t > 0, \tag{9}$$

where $\Omega = [0,L] \times [0,L] \in \mathbb{R}^{2+}$ and $\vec{n}$ is the outward unit normal vector to the boundary $\partial\Omega$.

4.1. Turing instability and Turing bifurcation

To analyze the spatio-temporal dynamics of the system (7) near the coexisting equilibrium state E_1^*, we focus on studying the diffusion-driven Turing instability in the diffusive system (7). We consider a small time and space dependent perturbations around the equilibrium state $E_1^*(X_1, Y_1) = E^*(X^*, Y^*)$ (say) as

$$\begin{pmatrix} X \\ Y \end{pmatrix} = \begin{pmatrix} X^* \\ Y^* \end{pmatrix} + \begin{pmatrix} X_n \\ Y_n \end{pmatrix} \exp\left(\lambda t + i(n \cdot \vec{\omega})\right), \tag{10}$$

where λ is the frequency at time t, n represents the wave-number and X_n, Y_n are the corresponding amplitudes. Substituting (10) into the system (7) and removing higher-order terms, we get the characteristic equation as:

$$|B_0 - n^2 D - \lambda I_2| = 0, \tag{11}$$

where I_2 is an identity matrix of order two, $D = \begin{pmatrix} d_{11} & 0 \\ 0 & d_{22} \end{pmatrix}$ is the matrix of diffusion coefficients and $B_0 = \begin{pmatrix} b_{11} & b_{12} \\ b_{21} & b_{22} \end{pmatrix}$ is the linearized matrix (6) evaluated at the equilibrium state E_1^*. The characteristic Eq. (11) can be written in simplified form as

$$\lambda^2 - \mathcal{T}_n \lambda + \mathcal{D}_n = 0, \quad n \in \mathbb{N} \cup \{0\}, \tag{12}$$

where $\mathcal{T}_n = Tr(B_0) - n^2(d_{11} + d_{22})$,

$$\mathcal{D}_n = (d_{11}d_{22})n^4 - (d_{11}b_{22} + d_{22}b_{11})n^2 + \det(B_0) \equiv \Lambda(n^2). \tag{13}$$

Here, $Tr(B_0) = b_{11} + b_{22}$ and $\det(B_0) = b_{11}b_{22} - b_{12}b_{21}$. The roots of characteristic Eq. (12) are $\lambda_{1,2}(n) = \frac{1}{2}\left(\mathcal{T}_n \pm \sqrt{\mathcal{T}_n^2 - 4\mathcal{D}_n}\right)$. The Turing instability arises when an equilibrium state, which is stable without diffusion, becomes unstable with diffusion. If the conditions $\mathcal{T}_n < 0$ and $\mathcal{D}_n > 0$ are satisfied, the system (7) is stable around the linearly stable equilibrium state E_1^* (we are in region R_2 as described in Table 1). At the equilibrium state E^*, $Tr(B_0) < 0$ due to the stability of non-diffusive system. So, the instability of diffusive system (7) does not depend upon $\mathcal{T}_n$ because $\mathcal{T}_n < 0$ for any natural number n. The only possible scenario in which the equilibrium state E_1^* can become unstable state of the diffusive system (7) is that $\mathcal{D}_n < 0$ for some n. This requires that the coefficient of n^2 in Eq. (13) must be positive. We want to establish a sufficient condition where the minimum of $\mathcal{D}_n$ is lower than zero. We observe that $\mathcal{D}_n$ attains its minimum at the critical value n_c^2, where $n_c^2 = \frac{d_{11}b_{22} + d_{22}b_{11}}{2d_{11}d_{22}}$. As a result, the requirement $\mathcal{D}_n$ at $n^2 = n_c^2$ transforms into

$$\frac{(d_{11}b_{22} + d_{22}b_{11})^2}{4(d_{11}d_{22})} > \det(B_0) \quad \text{with} \quad \mathcal{D}_n^{\min} = \frac{4(d_{11}d_{22})\det(B_0) - (d_{11}b_{22} + d_{22}b_{11})^2}{4(d_{11}d_{22})}.$$

We assume that $A_1 = (d_{11}b_{22} + d_{22}b_{11})$ and $A_2 = (d_{11}b_{22} + d_{22}b_{11})^2 - 4(d_{11}d_{22})\det(B_0)$, so that the conditions for Turing instability are given by:

(i) $Tr(B_0) < 0$ and $\det(B_0) > 0$: true as E_1^* is linearly stable (region R_2 Table 1),

(ii) $(d_{11}b_{22} + d_{22}b_{11})^2 > 4(d_{11}d_{22})\det(B_0) \implies \zeta > \sqrt{d_{11}d_{22}\mu\,(1 + fY^*)\det(B_0)}$, where $\zeta = d_{11}\epsilon\,\mu + d_{11}\epsilon\,\mu\,fY^* - d_{11}\epsilon^2 - d_{11}\epsilon^2 fY^* + d_{22}\epsilon - d_{22}\epsilon\,X^* - d_{22}\mu\,X^*$.

It is important to note that vanishing of the determinant $\mathcal{D}_n$ at some particular value of n gives rise to the emergence of a bifurcation in the space–time model (7), which is known as Turing bifurcation. We examine this bifurcation by taking $d_{22} = d_{22}^{[c]}$ as a bifurcation parameter obtained from $\mathcal{D}_n = 0$. Mathematically, the Turing bifurcation arises when $\mathcal{D}_n = 0$ and the transversality condition $\frac{d\,\mathcal{D}_n}{d\,d_{22}} \neq 0$ hold at $d_{22}^{[c]}$. Note that the equation $\mathcal{D}_n = 0$ possesses two positive roots, namely n_1^2 and n_2^2, which constitute the finite boundary wave numbers and satisfy the equation:

$$n_{2,1}^2 = \frac{A_1 \pm \sqrt{A_2}}{2d_{11}d_{22}}.$$

Differentiating Eq. (13) with respect to diffusion coefficient d_{22}, we get

$$\frac{d\,\mathcal{D}_n}{d\,d_{22}} = n^4 d_{11} - b_{11}n^2 = n^2(d_{11}n^2 - b_{11})\Big|_{n_{[c]}} \neq 0$$

if $d_{11}n_{[c]}^2 \neq b_{11}$, where $n_{[c]} = n_{2,1}$. Thus, the Turing bifurcation occurs in the system (7) if following hold:

$$d_{11}n_{[c]}^2 \neq b_{11} \quad \text{and} \quad d_{22}^{[c]} = \frac{b_{22}d_{11}n^2 - \det(B_0)}{n^2(d_{11}n^2 - b_{11})}.$$

Hence, we can conclude from above analysis that for some $n \neq 0$ $(0 < n_1^2 < n^2 < n_2^2)$ the Turing instability occurs.

In the top plot of Fig. 10, we present the Hopf bifurcation curve ($Tr(B_0) = 0$), Turing bifurcation curve ($D_n = 0$) and the different observed Turing patterns in the $(d_{22},\ f)$-plane, for the fixed values of the rest of parameters $\tau = 1$, $\mu = 0.95$, $\epsilon = 0.2$ (regions R_2 and R_3 when no diffusion is present), and $d_{11} = 2.5$. The intersection of the two bifurcation curves, Hopf and Turing, defines a Turing–Hopf bifurcation point. These two bifurcation curves divide the $(d_{22},\ f)$-plane into three main regions, namely Turing, Turing–Hopf and non-Turing. Turing region refers to the parameter regions where the equilibrium state is unstable to spatial dynamics but remains stable against temporal dynamics. Both Turing instability and Hopf bifurcation have occurred in the Turing–Hopf region (R_3) where the equilibrium state is unstable for both temporal and spatio-temporal dynamics and so, in this region, the system can exhibit a combination of spatial pattern formation (Turing) and temporal oscillations (Hopf). In addition, different types of patterns for the prey species of the top bifurcation diagram are illustrated in the bottom plots of Fig. 10. On that bifurcation diagram we have observed spot pattern, mixed patterns (with stripes and spots), approximately homogeneous (spots with small range of variation, see the color bar) and homogeneous (almost constant values). Note that the homogeneous case show variation in the figure but this is due to the small scale of the color bar, as the values are almost constant (the values of the no diffusion case for each set of parameters).

In Fig. 11, we study the influence of the fear parameter f on the determinant $\Lambda(n^2)$ of the diffusive system and the real component $Re(\lambda_n)$ of the eigenvalues for the spatio-temporal system (7) about the co-existing equilibrium state E_1^*. Fig. 11(a) shows that $\Lambda(n^2)$ becomes more and more negative when f increases and Fig. 11(b) shows the impact of f on the real component $Re(\lambda_n)$ of the characteristic root λ_n. The diagram illustrates that as the value of f increases, $Re(\lambda_n)$ progressively becomes more positive. However, the Turing pattern appears in the system when $f > 0.9316 = f_{[H]}$. Spatial–temporal patterns in a predator–prey model correspond to a non-uniform stationary state that is not amenable to analytical determination. As a result, computer simulations are required to comprehend the dynamic behavior of the proposed model. The goal of the next subsection is to use numerical simulations to understand how self-diffusion affects the system (3) when there are fear effects and an increasing functional response.

4.2. Numerical simulation of pattern formation

In order to study the practical consequences of the bifurcations in the model with diffusion, we analyze the spatio-temporal system (7) in a two dimensional spatial space $[0, 200] \times [0, 200]$. A fundamental practical distance in the predator–prey model is the average distance that an individual can travel and interact with another in a relevant period of time (e.g., a generation, a reproductive cycle). For a large predator (e.g., a wolf), this distance could be 10 kilometres. In our model, a "spatial unit" is defined by this range of interaction. A domain size of $[0, 200] \times [0, 200]$ was chosen to represent an area large enough to contain multiple patches of local populations, while remaining computationally manageable for parameter exploration.

In this article, we solve the PDE problem by means of a finite-differences numerical method with a spatial step size of $\Delta x = \Delta y = 1$ and a time step size $\Delta t = 0.025$. Starting with a homogeneous steady state, it takes time (the transient time) for patterns to become stationary reaching its asymptotic pattern. We perform pattern formation analysis to understand the effect of fear effect of predator and diffusion of each species.

Changing the fear parameter f:

Firstly, we investigate the asymptotic patterns caused just by changing the fear parameter f. As the value of fear –f– increases, it harms the evolution of the prey species and decrease in this parameter implies the prey density increases. This provides an intriguing motivation to examine the impact of fear parameter on the formation of patterns for the predator–prey species. To this goal, we fix

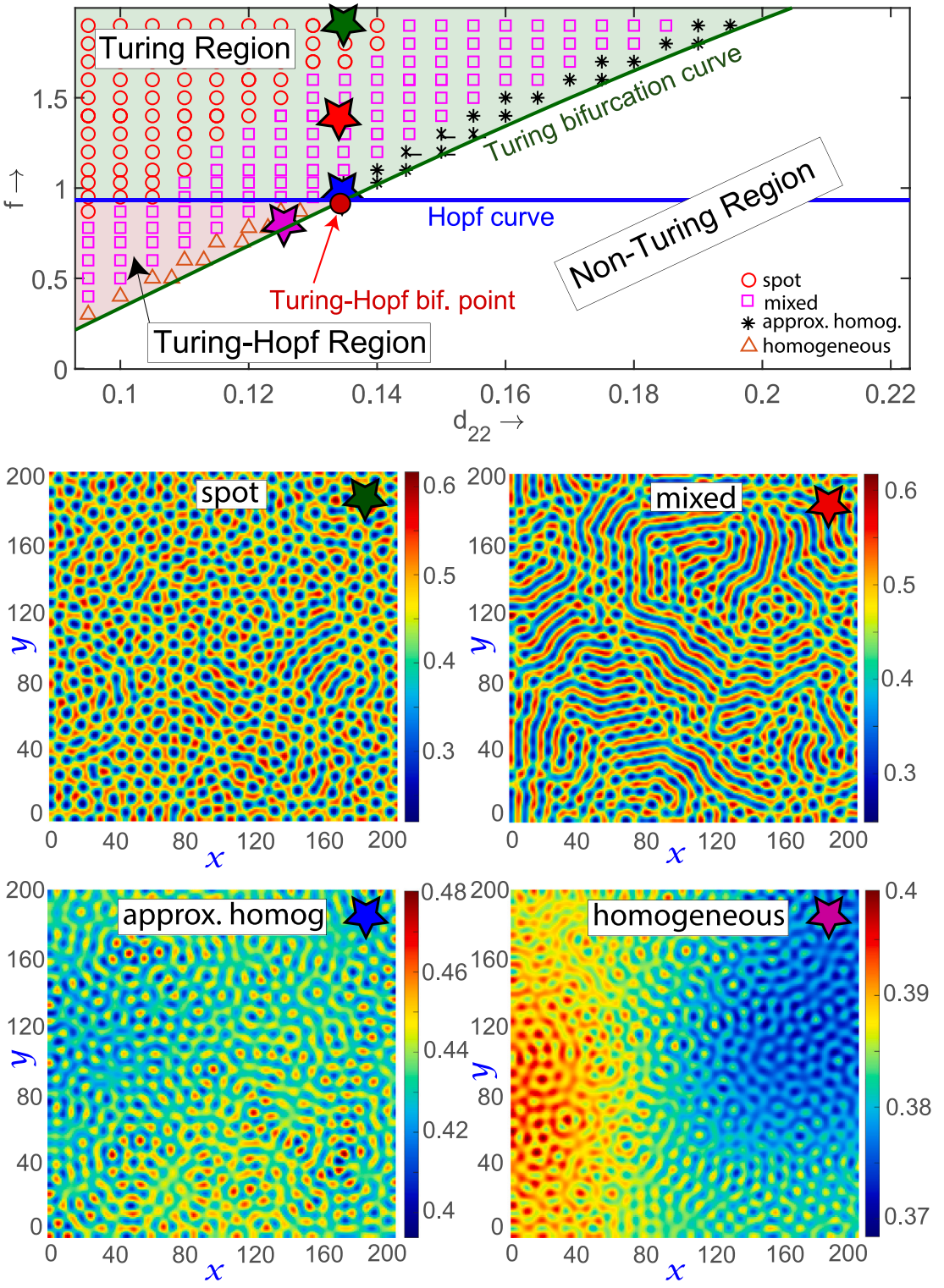

Fig. 10. Distribution of different types of patterns of system (7) in the (d_{22}, f) biparametric plane. The circle, square, star and triangle stand for spot, mixed, approximately homogeneous and homogeneous patterns, respectively. On the bottom plots we show examples of the Turing patterns for the prey species for the parameter values $(f, d_{22}) = (2, 0.1347)$ spot, $(f, d_{22}) = (1.4, 0.1347)$ mixed (stripe and spot), $(f, d_{22}) = (0.95, 0.1347)$ approx homogeneous and $(f, d_{22}) = (0.85, 0.129)$ homogeneous pattern.

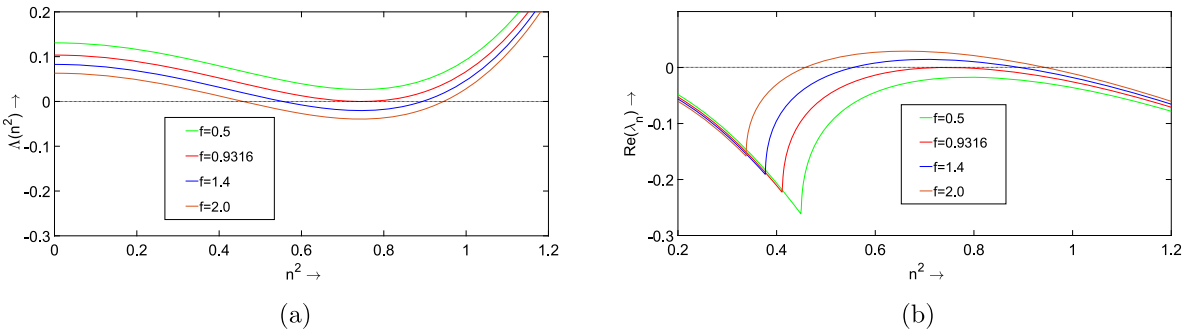

Fig. 11. For $\tau = 1$, $\mu = 0.95$, $\epsilon = 0.2$, $d_{11} = 2.5$ and $d_{22} = 0.1347$: (a) dispersion relation plot for various values of f, (b) plot of $Re(\lambda_n)$ with respect to n^2 for different values of f.

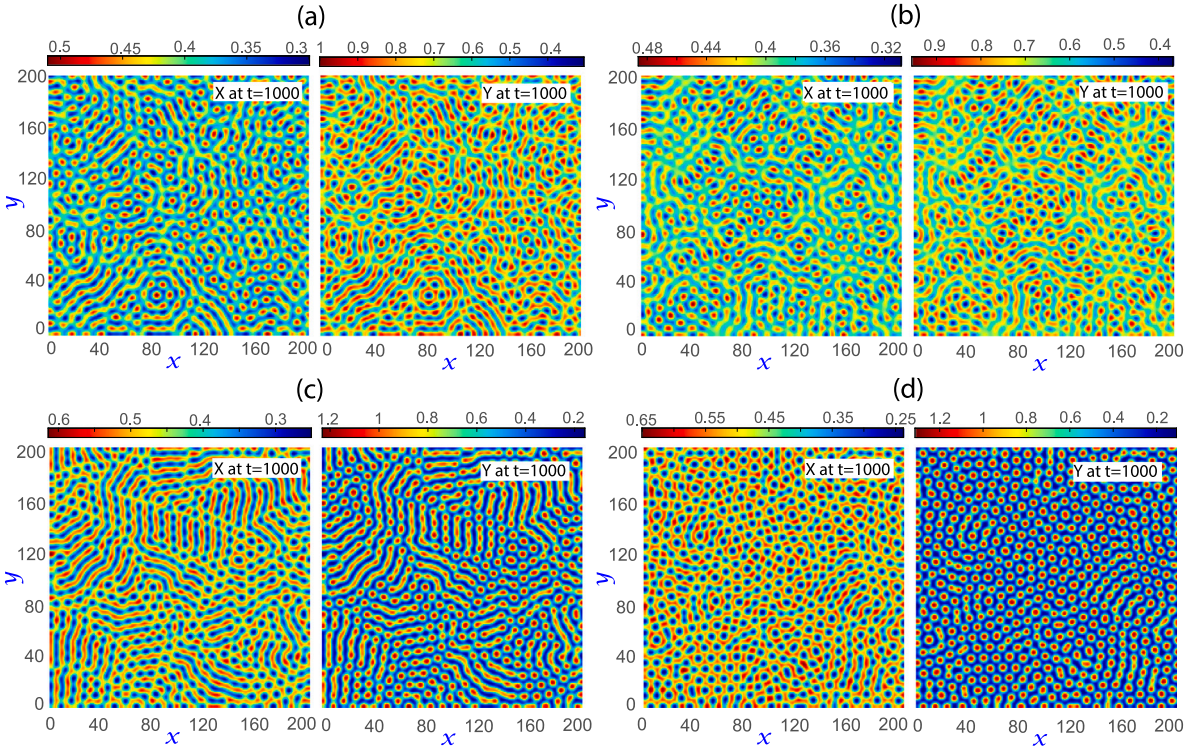

Fig. 12. Turing patterns for the prey (X) and predator (Y) species, in (a), (b) and (c) mixture of spot and strips for $f = 1$, $f = 1.25$ and $f = 1.5$, respectively, and in (d) spots for $f = 2$ (region R_2 in all cases).

the diffusion coefficients as $d_{11} = 2.5$ and $d_{22} = 0.13$ and the parameter in the region R_2 when no diffusion: $\tau = 1$, $\mu = 0.95$, $\epsilon = 0.2$. As fear parameter f increases from 1 to 2, we observe the emergence of the mixture of spot and stripe patterns, ending with red spots pattern of predator species at time $t = 1000$, as shown in Fig. 12(a) to Fig. 12(d). These spot and mixed type Turing patterns are inside the Turing region of Fig. 10. This mixed type pattern demonstrates a competition between strips and spots, where the spots eventually become dominant and evenly dispersed for f large. Thus, the increase in fear within the prey population due to the presence of predators reduces the prey's growth rate, as evidenced by the patterns showing a low prey density. Significantly, this leads to a temporary increase in the predator population, which cannot be sustained in the long term, as predators cannot survive without an adequate prey base. Hence, the ecological balance between prey and predators is ultimately disrupted, emphasizing the interconnected nature of their dynamics and the importance of stable environmental conditions to maintain population equilibrium. Fig. 12 presents the simulation results for both species, prey and predator, but we observe that they present the same pattern (reversed) but with different range of values in density. Therefore, in the following, we just plot the patterns for prey species to avoid repetition of the figures and without the color range bar and the space coordinates (in all cases they will be in the range $[0, 200]$).

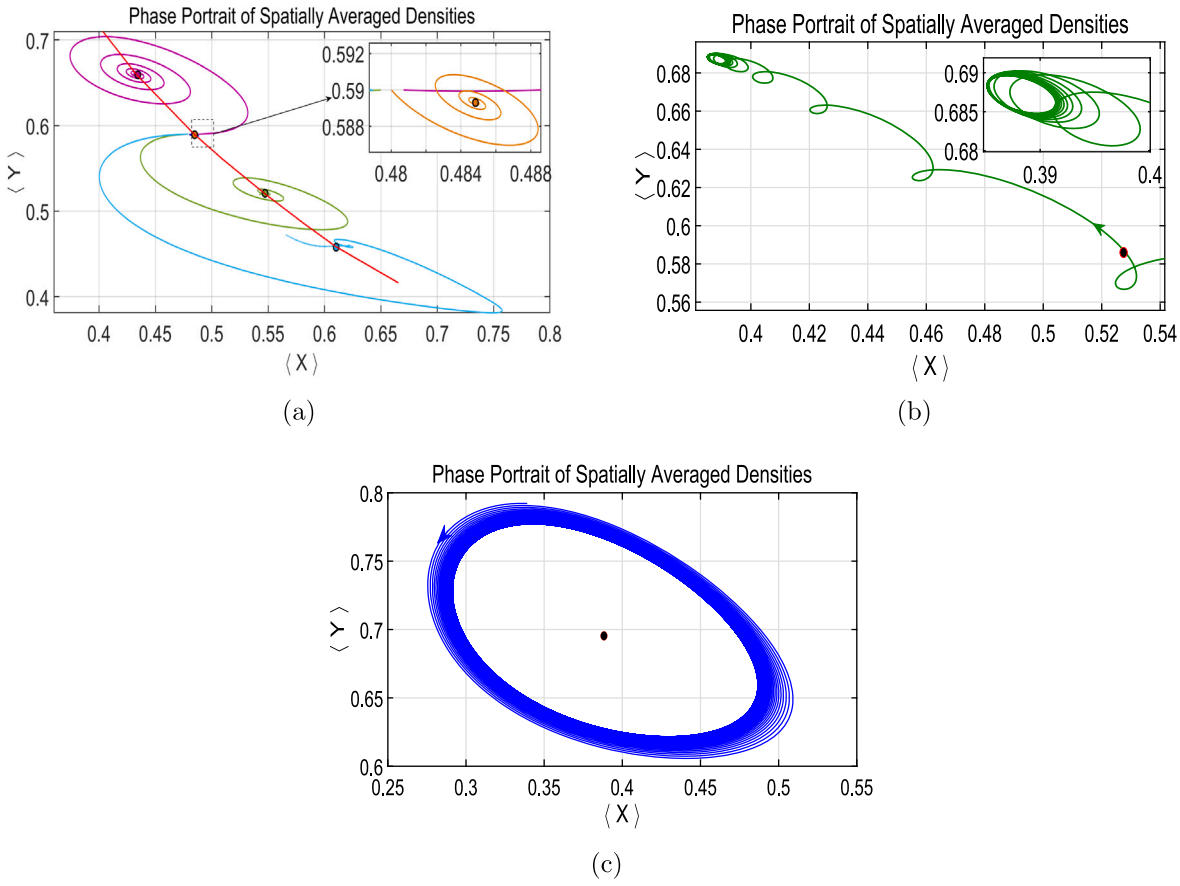

Fig. 13. Phase portrait of spatially averaged densities of prey X and predator Y species are plotted in (a) corresponding to Figs. 12, (b) at Turing–Hopf bifurcation point and (c) in Turing–Hopf region.

Furthermore, the average spatial densities corresponding to Fig. 12 are depicted in Fig. 13(a). For the data of the subfigures (a), (b), (c), and (d) of these figures, the phase portraits of the average spatial densities with respect to t are represented by pink, yellow, green, and blue colors, respectively. The red curve represents the variation in interior equilibrium with respect to the parameter f. These phase portraits indicate the spatial instability regions, highlighting the coexistence of both species in the domain over a long-term evolution. In these figures, the large dot represents the spatially homogeneous steady states (note that for each f the position of these steady states changes) to where each pattern converges. Moreover, for the parameters $f = 0.9316$, $\tau = 1$, $\mu = 0.95$, $\epsilon = 0.2$, and the diffusion constants $d_{11} = 2.5$ and $d_{22} = 0.1347$, we verify the existence of a Turing–Hopf bifurcation [Fig. 10]. At this bifurcation point, the phase portrait of the average densities is shown in Fig. 13(b). Note that is this case the pattern converges to a small periodic pattern (this point is close to the Turing–Hopf bifurcation point). Furthermore, for $f = 0.85$, $\tau = 1$, $\mu = 0.95$, $\epsilon = 0.2$, $d_{11} = 2.5$ and $d_{22} = 0.129$ (in the Turing–Hopf region), the phase portrait of the average densities is shown in Fig. 13(c). In this case the asymptotic pattern is a periodic pattern. Ecologically, it depicts a stable predator–prey periodic cycle in which prey growth drives predator increase, followed by prey decrease and predator reduction. This dynamic feedback maintains coexistence by emphasizing periodic population fluctuations rather than extinction or equilibrium stability in the Turing–Hopf region.

As an illustration of fixed and periodic patterns, in Fig. 14 we show some simulations in the Turing and Turing–Hopf regions to show the difference in the time evolution depending on the region. The top plots show the time evolution of the prey densities on one spatial line. The bottom plots show the time evolution of just one spatial point. At the Turing region the time evolution converges to a fixed pattern (plots (a) and (d)), while in the Turing–Hopf it converges to a periodic pattern (plots (b), (c), (e) and (f)).

Finally, and just as illustration, we plot some non-Turing patterns of the prey population, which are shown in Fig. 15 for some parameter values on the bifurcation diagram of Fig. 10. For lower predator diffusion rate ($d_{22} = 0.18$), the system produces an irregular speckled distribution characterized by irregular oscillations in prey density, indicating that strong predator mobility can destabilize the prey population [Fig. 15(a)]. As the predator diffusion rate is slightly enhanced ($d_{22} = 0.2$), the prey density organizes into a localized hot spot, reflecting nonlinear prey–predator feedback and wave-like instabilities rather than diffusion-driven Turing mechanisms [Fig. 15(b)]. Furthermore, at lower prey diffusion rate ($d_{11} = 0.5$), the system maintains a nearly uniform background

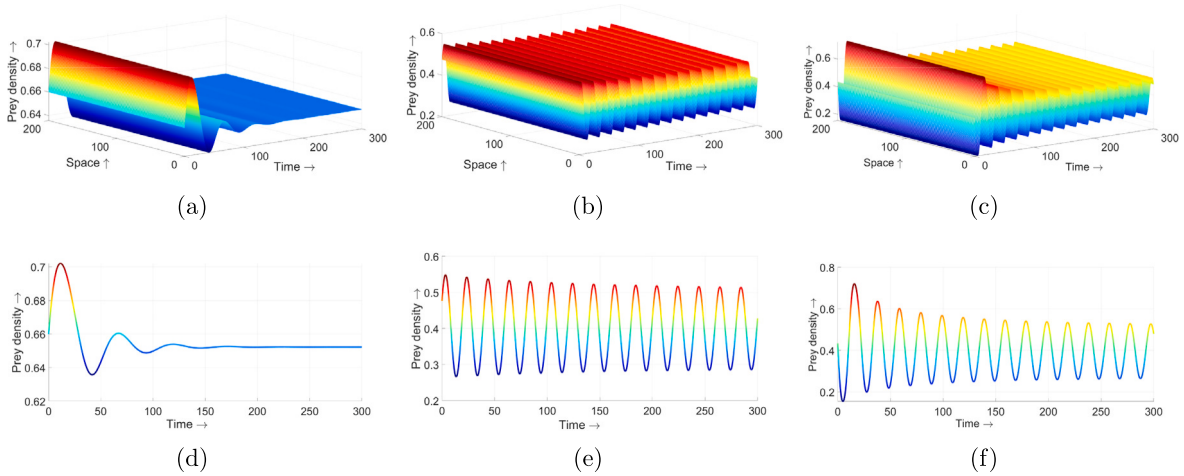

Fig. 14. Time-spatial simulation using the fixed values $\tau = 1$, $\mu = 0.95$ and $\epsilon = 0.2$, $d_{11} = 2.5$. (a) and (d) Numerical simulation in Turing region for prey species for $f = 3.0$ and $d_{22} = 0.1347$. (b) and (e) Numerical simulation close to the Turing–Hopf bifurcation point and inside the Turing–Hopf region for prey species for $f_{[H]} = 0.9316$ and $d_{22} = 0.1347$. (c) and (f) Numerical simulation inside the Turing–Hopf region for prey species for $f = 0.85$, $d_{22} = 0.129$.

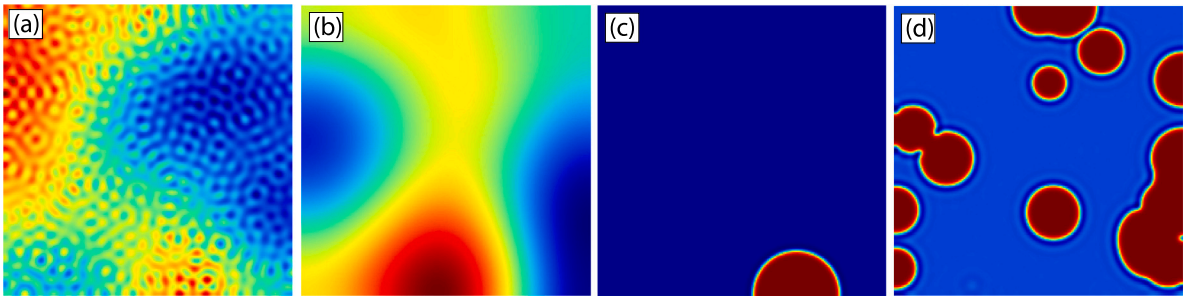

Fig. 15. Non-Turing patterns shown by prey species. Parameter values are (a) $d_{22} = 0.18$ and (b) $d_{22} = 0.2$ with $f = 1$, $\tau = 1$, $\mu = 0.95$, $\epsilon = 0.2$, $d_{11} = 2.5$, (c) $d_{11} = 0.5$ and (d) $d_{11} = 0.8$ with $f = 1.2$, $\tau = 1.2$, $\mu = 0.95$, $\epsilon = 0.2.$, $d_{22} = 0.15$.

with an isolated prey cluster, suggesting that limited prey dispersal supports the persistence of solitary localized populations [Fig. 15(c)]. Multiple circular clusters emerge, resembled prey droplets that highlight the coexistence of prey-rich and prey-poor regions with a moderately higher prey diffusion rate ($d_{11} = 0.8$) [Fig. 15(d)].

Changing the diffusion coefficient (d_{11})**:**

Now, we study the changes when the diffusion coefficient d_{11} is used as the bifurcation parameter. In Fig. 16 we show in the top plot a bifurcation diagram on a parametric line d_{11} due to the pure Turing instability mechanism, with all other parameters fixed as $f = 1.2$, $\tau = 1.2$, $\mu = 0.95$, $\epsilon = 0.23$ (region R_2 when no diffusion), and $d_{22} = 0.15$.

We have observed in Fig. 16 similar patterns as in Fig. 10. We add the labyrinth terminology for the mixed cases where the stripes are more connected giving rise to "labyrinths". Moreover, on the bottom plots, we illustrate the obtained patterns. Traditional patterns appear for different values of diffusion parameter of prey d_{11} due to the pure Turing instability mechanism, with all other parameters fixed as $f = 1.2$, $\tau = 1.2$, $\mu = 0.95$, $\epsilon = 0.23$ (region R_2 when no diffusion), $d_{22} = 0.15$ at time $t = 500$. As prey diffusion coefficient d_{11} increases from 1 to 3, the mixture of cold labyrinth and spot patterns changes from labyrinth to spot patterns. In this case we denote as approx. homogeneous pattern to the case where most of the space distribution presents the same density value in spite of having some structures (like in the example shown in Fig. 16). Ecologically, an increase in the movement of the prey population can reduce their numbers, as higher prey density region decreases with increased movement. This, in turn, results in an increase in the predator population.

5. Conclusion

The process of predator–prey interaction is a fundamental subject in the fields of ecology and adaptive biology. The survival of predator species is determined by their consumption process and hunting methods for prey. The predator's consuming process is determined by the size of the resource, its availability, and defensive mechanism of the resource. Both species use distinct techniques

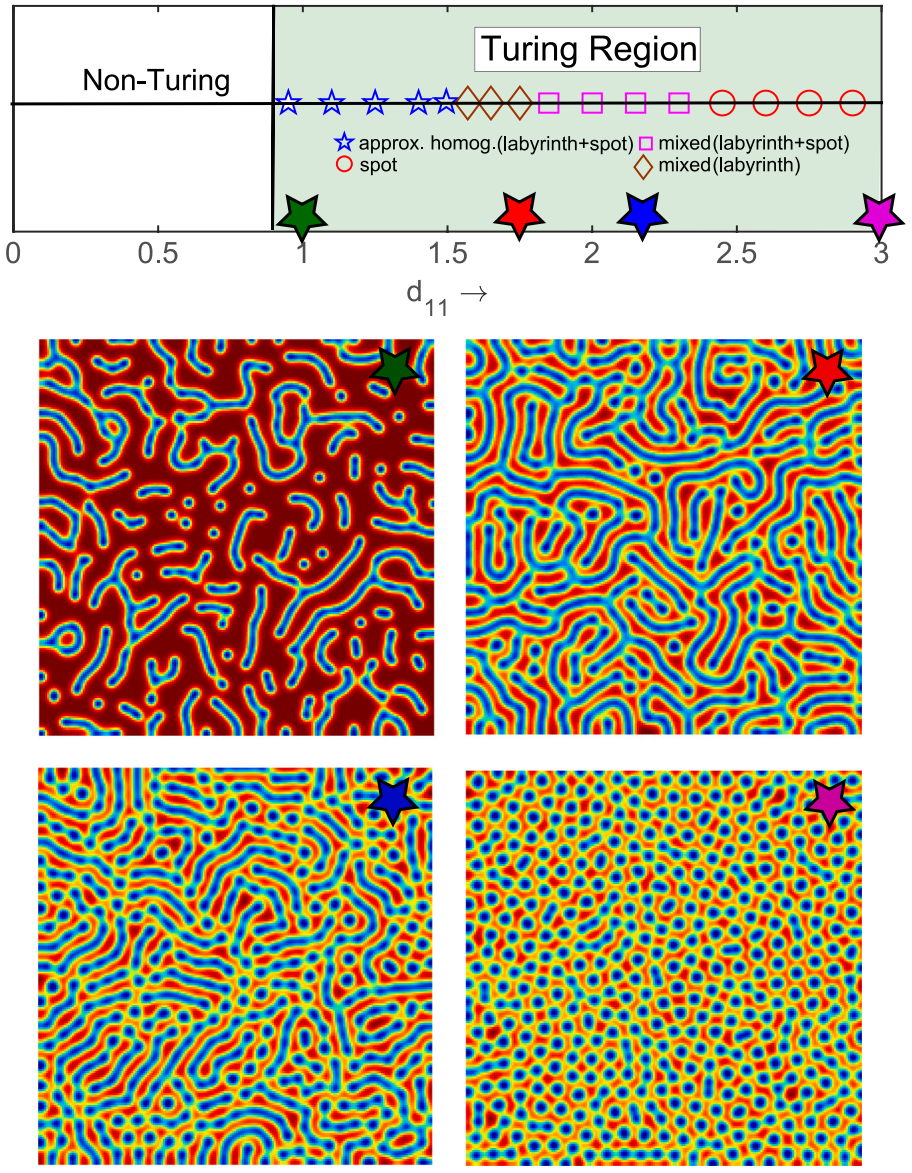

Fig. 16. Top: different types of Turing patterns for changing d_{11} with fixed $f = 1.2$, $\tau = 1.2$, $\mu = 0.95$, $\epsilon = 0.23$ and $d_{22} = 0.15$ (region R_2 when no diffusion is present). Bottom: examples of the Turing patterns shown by prey species for $d_{11} = 1$, $d_{11} = 1.75$, $d_{11} = 2.15$ and $d_{11} = 3.0$.

to optimize their density. Several types of predators work together while hunting to enhance the probability of catching their prey. The functional response reveals the effect of predators forming spatial groups on the encounter-rate between predators and prey. This explains a scenario of cooperative hunting, where a group of predators moves in a line formation, locates, and then hunts a herd or school of prey. Such cooperative hunting behavior, where predators hunt in line formation, fear phenomena arise in the prey population. Therefore, the system plays a more significant role after including the fear effect in the prey population.

In this article, we study the diffusive and non-diffusive predator–prey system with fear effect and increasing type of functional response. Here, the predator's fear component is considered, which results in a decrease in the overall population of prey. First, we examine the proposed non-spatial predator–prey system. We provide an analysis of the positivity and boundedness of solutions for both scenarios: when the predator mortality rate is below and over the carrying capacity of the prey population. We examined the presence of all non-negative equilibrium states and their local stability. We show that the predator-free equilibrium state $E_k(1, 0)$ becomes globally asymptotically stable when the system (3) does not have any feasible interior equilibrium state. We demonstrated that predator species became extinct when their consumption rate exceeds the threshold value. Ecologically, this condition may be interpreted as follows: predators' high consumption rate diminishes prey density too much, causing them to go extinct due to their inability to find prey. We displayed that equilibrium states $E_0(0, 0)$ and $E_2^*(X_2, Y_2)$ are always saddle points. In contrast, the

equilibrium state $E_1^*(X_1, Y_1)$ can be a saddle point or an attractor based on parametric restriction. Furthermore, a separatrix curve that splits the basins of attraction of $E_k(1,0)$ and $E_1^*(X_1, Y_1)$ is determined by the stable manifold of the equilibrium state $E_2^*(X_2, Y_2)$ [see Fig. 9]. It implies that proposed system (3) admits the bistability behavior between $E_k(1,0)$ and the co-existing equilibrium state $E_1^*(X_1, Y_1)$. We studied the Hopf bifurcation with respect to the fear parameter f, the saddle–node bifurcation about the double root of the polynomial $p(X)$ [(4)] and we also showed numerically that the system undergoes a Bogdanov–Takens bifurcation about the unique double equilibrium state $\bar{E}$ depending on f and ϵ. Additionally, we plot the two parametric bifurcation diagram for various parameters [see Fig. 7] obtained with continuation techniques.

Further, we focus on the influence of diffusion on the proposed model about the coexisting steady state. We establish the criteria for Turing instability, which leads to instability when diffusion is added, and find the range of wave numbers for instability analytically. We conduct several simulations in Turing domain to better understand species movement and allocation in the spatial domain over time. In the Turing region, patterns associated with three key parameters f, d_{11} and d_{22} are observed. Predators and prey employ various strategies to enhance their biomass. Numerous predators cooperate during hunting to increase their success in capturing prey and ensure efficient consumption, thus increasing the carrying capacity of their population. On the other hand, due to the fear of predation, prey engage in various anti-predator behaviors as survival strategies, leading to a decline in the birth rates of prey populations. Ecologically, it is worth noting that the density of both populations decreases as hunting cooperation and fear factors increase. The impact of variations in diffusion coefficients and the level of fear factor $-f-$, on pattern formation is reported in the spatially extended model (7) and the conclusions are outlined below:

1. If the level of fear factor $-f-$ is varied, then the spatio-temporal system (7) demonstrates a shift in pattern transmission from a mixture of spots and stripes to red spots [Fig. 12]. As a result, the density of the prey population decreases as the level of fear induced by predators increases, potentially destabilizing the ecosystem. Therefore, an excessive increase in fear is detrimental to maintaining a healthy ecosystem.
2. The spatio-temporal system shows the labyrinth pattern which is changed to spots via stripes as we increase the value of d_{11} [Fig. 16]. Ecologically, it is reflects that an increased movement rate might reduce the local density of prey, but it could also contribute to a more stable overall population if it aids in survival and resource distribution.

From an ecological perspective, the fear effect plays a dual role in predator–prey dynamics. If the level of fear becomes excessively high, it destabilizes the ecosystem, potentially leading to the extinction of predators or both predators and prey. However, a moderate level of fear can enhance the balance and interactions between the two populations, supporting their coexistence and long-term survival within the ecosystem. As a future research direction, the present spatio-temporal predator–prey model may be extended to its fractional-order form. The fractional-order framework [55,56] can better capture memory and hereditary characteristics in ecological systems, potentially altering oscillatory onset and stability boundaries. Hence, reformulating the current model as a fractional-order delayed reaction–diffusion system would provide valuable insights into how the fractional derivative order governs the emergence and stability of spatio-temporal patterns. Other possible future lines are the use of control techniques to ensure ecosystem balance like in [54] or to link this model with data-driven techniques to provide a model tailored to specific realistic values [45].

CRediT authorship contribution statement

R.P. Gupta: Writing – review & editing, Writing – original draft, Visualization, Supervision, Methodology, Investigation, Funding acquisition, Formal analysis, Conceptualization. **Harinand Singh:** Writing – review & editing, Writing – original draft, Visualization, Validation, Software, Methodology, Investigation, Formal analysis, Conceptualization. **Roberto Barrio:** Writing – review & editing, Visualization, Supervision, Methodology, Investigation, Funding acquisition, Conceptualization. **Arun Kumar:** Writing – review & editing, Writing – original draft, Visualization, Validation, Methodology, Investigation, Formal analysis, Conceptualization.

Declaration of competing interest

The authors declare that they have no known competing financial interests or personal relationships that could have appeared to influence the work reported in this paper.

Acknowledgments

R.P. Gupta acknowledges the support from BHU, India for Trans-Disciplinary project grant (Ref. No. R/Dev./D/IoE/Trans-Disciplinary Research/2023-24/60570-60572) under the IoE scheme. H. Singh is thankful to UGC for the financial support under the CSIR-UGC JRF (NTA Ref No.: 211610002214). R. Barrio has been supported by the Spanish Research projects PID2021-122961NB-I00 and PID2024-156032NB-I00, and the European Regional Development Fund and Diputación General de Aragón (E24-23R and LMP94-21 grants).

Data availability

Data sharing is not applicable to this article as no new data were created or analyzed in this study.

References

[1] P. Turchin, Complex Population Dynamics: A Theoretical/Empirical Synthesis (MPB-35), Princeton University Press, 2013.
[2] T. Li, Q. Wang, Turing patterns in a predator-prey reaction-diffusion model with seasonality and fear effect, J. Nonlinear Sci. 33 (5) (2023) 86.
[3] Z. Ma, J. Wang, Bifurcation analysis of a multiple-delayed predator–prey system with habitat complexity, Int. J. Bifurcat. Chaos 34 (16) (2024) 2450198.
[4] G. Mandal, L.N. Guin, S. Chakravarty, Complex patterns in a reaction–diffusion system with fear and anti-predator responses, Int. J. Bifurcat. Chaos 34 (12) (2024) 2450154.
[5] L. Marton, K.M. Hangos, A. Magyar, Passivity of Lotka–Volterra and quasi-polynomial systems, Nonlinearity 34 (4) (2021) 1880.
[6] M. Kot, Elements of Mathematical Ecology, Cambridge University Press, 2001.
[7] Y. Zeng, P. Yu, Multistable states in a predator–prey model with generalized holling type III functional response and a strong Allee effect, Commun. Nonlinear Sci. Numer. Simul. 131 (2024) 107846.
[8] X. Sun, R. Yuan, L. Wang, Bifurcations in a diffusive predator–prey model with Beddington–DeAngelis functional response and nonselective harvesting, J. Nonlinear Sci. 29 (2019) 287–318.
[9] S.N. Karim, T.K. Ang, Co-dimension 2 bifurcation analysis of a tri-trophic food chain model with strong Allee effect and Crowley–Martin functional response, Chaos Solitons Fractals 186 (2024) 115316.
[10] C. Cosner, D.L. DeAngelis, J.S. Ault, D.B. Olson, Effects of spatial grouping on the functional response of predators, Theor. Popul. Biol. 56 (1) (1999) 65–75.
[11] C.S. Holling, Some characteristics of simple types of predation and parasitism, Can. Entomol. 91 (7) (1959) 385–398.
[12] M.D. Breed, J. Moore, Animal Behavior, Academic Press, 2022.
[13] R. Bshary, A. Hohner, K. Ait-el Djoudi, H. Fricke, Interspecific communicative and coordinated hunting between groupers and giant moray eels in the red sea, PLoS Biol. 4 (12) (2006) 2393–2398.
[14] J.O. Coulson, T.D. Coulson, Reexamining cooperative hunting in Harris's Hawk (Parabuteo unicinctus): large prey or challenging habitats? Auk 130 (3) (2013) 548–552.
[15] S. Creel, N. Creel, Communal hunting and pack size in African wild dogs, lycaon-pictus, Anim. Behav. 50 (5) (1995) 1325–1339.
[16] D. Hector, Cooperative hunting and its relationship to foraging succes and prey size in an avian predator, Ethology 73 (3) (1986) 247–257.
[17] N.J. Mooney, Co-operative hunting in the brown falcon falco berigora, Corella 13 (1989) 18–21.
[18] P. Schmidt, L. Mech, Wolf pack size and food acquisition, Amer. Nat. 150 (4) (1997) 513–517.
[19] M. Clinchy, M.J. Sheriff, L.Y. Zanette, Predator-induced stress and the ecology of fear, Funct. Ecol. 27 (1) (2013) 56–65.
[20] S. Creel, D. Christianson, S. Liley, J.A. Winnie Jr., Predation risk affects reproductive physiology and demography of elk, Science 315 (5814) (2007) 960-960.
[21] X. Wang, L. Zanette, X. Zou, Modelling the fear effect in predator–prey interactions, J. Math. Biol. 73 (5) (2016) 1179–1204.
[22] A. Das, G.P. Samanta, Modeling the fear effect on a stochastic prey-predator system with additional food for the predator, J. Phys. A 51 (46) (2018) 465601.
[23] K. Sarkar, S. Khajanchi, Impact of fear effect on the growth of prey in a predator–prey interaction model, Ecol. Complex 42 (2020) 100826.
[24] Sajan Anshu, B. Dubey, Bifurcation analysis and spatiotemporal dynamics in a diffusive predator–prey system incorporating a holling type II functional response, Int. J. Bifurcat. Chaos 34 (08) (2024) 2450105.
[25] S. Li, J. Wu, Y. Dong, Effects of degeneracy and response function in a diffusion predator–prey model, Nonlinearity 31 (4) (2018) 1461.
[26] A.M. Turing, A reaction–diffusion model for development, The chemical basis of morphogenesis, Philos. Trans. R. Soc. B 237 (641) (1990) 37–72.
[27] L.A. Segel, J.L. Jackson, Dissipative structure: an explanation and an ecological example, J. Theoret. Biol. 37 (3) (1972) 545–559.
[28] B. Li, L. Zhu, Turing instability analysis of a reaction–diffusion system for rumor propagation in continuous space and complex networks, Inf. Process. Manag. 61 (3) (2024) 103621.
[29] H. Sha, L. Zhu, Dynamic analysis of pattern and optimal control research of rumor propagation model on different networks, Inf. Process. Manag. 62 (3) (2025) 104016.
[30] J. Shi, L. Zhu, Turing pattern theory on homogeneous and heterogeneous higher-order temporal network system, J. Math. Phys. 66 (4) (2025).
[31] T. Yang, L. Zhu, S. Shen, L. He, Pattern dynamics analysis and parameter identification of spatiotemporal infectious disease models on complex networks, Math. Biosci. (2025) 109502.
[32] L. Zhu, T. Zheng, Pattern dynamics analysis and application of west nile virus spatiotemporal models based on higher-order network topology: L. Zhu, T. Zheng, Bull. Math. Biol. 87 (9) (2025) 121.
[33] S.K. Sasmal, Anshu, B. Dubey, Diffusive patterns in a predator–prey system with fear and hunting cooperation, Eur. Phys. J. Plus 137 (2) (2022) 281.
[34] D. Song, C. Li, Y. Song, Stability and cross-diffusion-driven instability in a diffusive predator–prey system with hunting cooperation functional response, Nonlinear Anal. Real World Appl. 54 (2020) 103106.
[35] D. Pal, D. Kesh, D. Mukherjee, Cross-diffusion mediated spatio-temporal patterns in a predator–prey system with hunting cooperation and fear effect, Math. Comput. Simulation 220 (2024) 128–147.
[36] S. Pal, N. Pal, S. Samanta, J. Chattopadhyay, Fear effect in prey and hunting cooperation among predators in a Leslie–Gower model, Math. Biosci. Eng. 16 (5) (2019) 5146.
[37] K. Ryu, W. Ko, M. Haque, Bifurcation analysis in a predator–prey system with a functional response increasing in both predator and prey densities, Nonlinear Dynam. 94 (2018) 1639–1656.
[38] Q. Liu, D. Jiang, Influence of the fear factor on the dynamics of a stochastic predator–prey model, Appl. Math. Lett. 112 (2021) 106756.
[39] N. Mondal, S. Paul, A. Mahata, M.A. Biswas, B. Roy, S. Alam, Study of dynamical behaviors of harvested stage-structured predator–prey fishery model with fear effect on prey under interval uncertainty, Frankl. Open 6 (2024) 100060.
[40] Z. Shang, Y. Qiao, Complex dynamics of a quad-trophic food chain model with Beddington–DeAngelis functional response, fear effect and prey refuge, Qual. Theory Dyn. Syst. 24 (1) (2025) 50.
[41] S.K. Sasmal, Population dynamics with multiple Allee effects induced by fear factors–A mathematical study on prey-predator interactions, Appl. Math. Model. 64 (2018) 1–14.
[42] Y. Shi, J. Wu, Q. Cao, Analysis on a diffusive multiple Allee effects predator–prey model induced by fear factors, Nonlinear Anal. Real World Appl. 59 (2021) 103249.
[43] L.Y. Zanette, A.F. White, M.C. Allen, M. Clinchy, Perceived predation risk reduces the number of offspring songbirds produce per year, Science 334 (6061) (2011) 1398–1401.
[44] K.H. Elliott, G.S. Betini, D.R. Norris, Fear creates an Allee effect: experimental evidence from seasonal populations, Proc. R. Soc. B Biol. Sci. 284 (1857) (2017) 20170878.
[45] L. Zhu, Y. Ding, S. Shen, Green behavior propagation analysis based on statistical theory and intelligent algorithm in data-driven environment, Math. Biosci. 379 (2025) 109340.
[46] J. Lin, C. Xu, Y. Xu, Y. Zhao, Y. Pang, Z. Liu, J. Shen, Bifurcation and controller design in a 3D delayed predator–prey model, AIMS Math. 9 (12) (2024) 33891–33929.

[47] J. Lin, C. Xu, Y. Zhao, Q. Deng, Hopf bifurcation and controller design for a predator–prey model with double delays, AIP Adv. 15 (7) (2025).
[48] Y. Zhao, C. Xu, Y. Xu, J. Lin, Y. Pang, Z. Liu, J. Shen, Mathematical exploration on control of bifurcation for a 3D predator–prey model with delay, AIMS Math. 9 (11) (2024) 29883–29915.
[49] G. Birkhoff, G.C. Rota, Ordinary Differential Equations, Ginn, Boston, 1982.
[50] L. Perko, Differential Equations and Dynamical Systems, Springer, New York, 1996.
[51] D.R. Merkin, Introduction to the Theory of Stability, in: Text in Applied Mathematics, vol. 24, Springer, Berlin, 1997.
[52] Yu A. Kuznetsov, Elements of Applied Bifurcation Theory, Springer, 2004.
[53] A. Dhooge, W. Govaerts, Y.A. Kuznetsov, MATCONT: a MATLAB package for numerical bifurcation analysis of ODEs, ACM Trans. Math. Softw. (TOMS) 29 (2) (2003) 141–164.
[54] P. Rebelo, S. Rosa, An optimal control problem for a predator–prey model with strong and weak preys, Chaos Solitons Fractals 191 (2025) 115838.
[55] Q. Cui, C. Xu, Y. Xu, W. Ou, Y. Pang, Z. Liu, U. Ghosh, Bifurcation and controller design of 5D BAM neural networks with time delay, Int. J. Numer. Model.: Electron. Netw. Devices Fields 37 (6) (2024) e3316.
[56] P. Li, R. Gao, C. Xu, Y. Li, A. Akgül, D. Baleanu, Dynamics exploration for a fractional-order delayed zooplankton–phytoplankton system, Chaos Solitons Fractals 166 (2023) 112975.